Quantification of Pacific Plate Hotspot Tracks Since 80 Ma and the Relative Timing of Eocene Plate Tectonic Events

Kevin Mitchell Gaastra[1,1], Richard G. Gordon[1,1], and Daniel Woodworth[1,1]

[1]Rice University

November 30, 2022

Abstract

The motion of the Pacific plate relative to Pacific hotspots produces age-progressive chains of volcanoes. New methods of analysis of volcano locations and age dates using a small number of adjustable parameters (10 per chain) are presented. Simple fits to age progressions along Pacific hotspot chains indicate 1σ age uncertainties of $\approx\pm$1.0 to $\pm$3.0 Ma. Motion between the Hawaii and Louisville hotspots differs insignificantly from zero with rates of 2$\pm$4 mm/a (=$\pm$2σ) for 0–48 Ma and 26$\pm$34 mm/a (=$\pm$2σ) for 48–80 Ma. Relative to a mean Pacific hotspot reference frame, motions of the Hawaii, Louisville, and Rurutu hotspots are also insignificant. Therefore plumes underlying these Pacific hotspots may be more stable in a convecting mantle than previously inferred. We find no significant difference in age between the Eocene bends of the Pacific hotspot chains. The best-fitting assumed-coeval age for the bends is 47.4$\pm$1.0 Ma (=$\pm$2σ), coincident with the initiation of the doubling of the spreading rate of the Pacific plate relative to the Farallon and Vancouver plates. The initiation of the Eocene slowdown of India preceded the bends and was completed after the bends. Any causal relation of this slowdown to the Hawaiian-Emperor bend remains obscure. On the other hand, initiation of subduction of the Pacific plate in the west and southwest Pacific Ocean Basin likely preceded the formation of the bends, consistent with subduction initiation changing the torque on the Pacific plate such that it started moving in a more westward direction thus creating the Hawaiian-Emperor Bend.

Quantification of Pacific Plate Hotspot Tracks Since 80 Ma and the Relative Timing of Eocene Plate Tectonic Events

Kevin M. Gaastra[1], Richard G. Gordon[1], and Daniel T. Woodworth[1]

[1]Department of Earth, Environmental, and Planetary Sciences, Rice University, Houston, Texas USA

Key Points:

- Rates of Louisville-Hawaii hotspot motion are 2±4 mm/a for 0–48 Ma and 26±34 mm/a for 48–80 Ma
- No significant difference in ages of Hawaiian-Emperor and Louisville bends, which have a maximum likelihood combined age of 47.4 ± 1.0 Ma
- Initiation of Pacific-plate subduction in the west and southwest Pacific Ocean Basin likely preceded formation of the bends by several Ma

Corresponding author: Kevin Gaastra, `kmg9@rice.edu`

Abstract

The motion of the Pacific plate relative to Pacific hotspots produces age-progressive chains of volcanoes. New methods of analysis of volcano locations and age dates using a small number of adjustable parameters (10 per chain) are presented. Simple fits to age progressions along Pacific hotspot chains indicate 1σ age uncertainties of $\approx \pm 1.0$ to ± 3.0 Ma. Motion between the Hawaii and Louisville hotspots differs insignificantly from zero with rates of 2 ± 4 mm/a ($= \pm 2\sigma$) for 0–48 Ma and 26 ± 34 mm/a ($= \pm 2\sigma$) for 48–80 Ma. Relative to a mean Pacific hotspot reference frame, motions of the Hawaii, Louisville, and Rurutu hotspots are also insignificant. Therefore plumes underlying these Pacific hotspots may be more stable in a convecting mantle than previously inferred. We find no significant difference in age between the Eocene bends of the Pacific hotspot chains. The best-fitting assumed-coeval age for the bends is 47.4 ± 1.0 Ma ($= \pm 2\sigma$), coincident with the initiation of the doubling of the spreading rate of the Pacific plate relative to the Farallon and Vancouver plates. The initiation of the Eocene slowdown of India preceded the bends and was completed after the bends. Any causal relation of this slowdown to the Hawaiian-Emperor bend remains obscure. On the other hand, initiation of subduction of the Pacific plate in the west and southwest Pacific Ocean Basin likely preceded the formation of the bends, consistent with subduction initiation changing the torque on the Pacific plate such that it started moving in a more westward direction thus creating the Hawaiian-Emperor Bend.

Plain Language Summary

Volcanic island chains in the Pacific Ocean, formed by rising plumes of mantle rock (hotspots), exhibit peculiar bends. To better understand the tectonic processes represented by these bends we examine the relative timing of major tectonic events during the Eocene. Here we examine the age progression of the submarine and subaerial volcanic edifices left by three prominent Pacific plate hotspots, all thought to have changed volcanic propagation direction $\approx$47–51 million years ago (Ma). We construct a simple model of their location and age progression from 80 million years ago to present and from this we find that rates of motion between these hotspots are insignificant and are likely to be smaller than previously thought. In addition, we find no difference in age of the bends of these three hotspot tracks and determine their age as 47.4 ± 1 Ma. Finally, we note that initiation of western and southwestern Pacific subduction of the Pacific plate

preceded the bends, consistent with the pull on the Pacific plate caused by subduction initiation causing the change in Pacific plate motion, which–in turn–caused the change in trend.

1 Introduction

Hotspot volcanoes are widely thought to be the surface manifestation of mantle plumes, upwellings of solid rock sourced from deep in the mantle (J. T. Wilson, 1963; Morgan, 1972). Early observations of the age progression of volcanoes constructed atop a tectonic plate moving relative to an individual hotspot indicated a monotonic increase in age away from the site of present volcanism. The age progressions and the geometry of the resulting chains of hotspot volcanoes are used to reconstruct plate motions relative to the deep mantle (Morgan, 1981). The estimated motions rely on the assumption that the hotspots are approximately fixed laterally relative to each other and relative to the deep mantle over long intervals of time. This assumption, known as the fixed-hotspot hypothesis, has been challenged using many different types of data and models (Molnar & Stock, 1987; Steinberger & O'Connell, 1998; Raymond et al., 2000; Tarduno et al., 2003), but some of these challenges have been shown to be fatally flawed (Andrews et al., 2006; Koivisto et al., 2014). How fast hotspots move relative to each other is central for understanding absolute plate motions, true polar wander, and the nature of mantle circulation (Wessel & Kroenke, 2008; Doubrovine et al., 2012; Koivisto et al., 2014; Wang et al., 2017, 2019a, 2019b; McKenzie, 2018).

Wessel and Kroenke (2009) used geographic and age progressions of Pacific-plate hotspot tracks to test hotspot fixity and to estimate a bound on the magnitude of interhotspot motion. Age dates were linearly interpolated to produce a continuous age model. No significant motion was inferred for 50 Ma to present for any hotspot pair, but $\approx 5^\circ \pm 2^\circ$ of nominal convergence was inferred from 80 to 50 Ma between the Hawaii and Louisville hotspots.

Recent investigation of the age progression along the previously undated track of the Rurutu hotspot contributes important data for estimating motion between three Pacific hotspots: Hawaii, Louisville, and Rurutu (Konrad et al., 2018). To analyze the age progressions of the tracks of these three hotspots, Konrad et al. (2018) employ a piecewise cubic hermite interpolating function. Modeling hotspot propagation with their approach requires the path be smooth and monotonic to fit the data perfectly with $n = 4(N-1)$ adjustable parameters for N data (Fritsch & Carlson, 1980). For the data of Konrad et al. (2018), n is 88 for the Emperor chain, 84 for the Louisville chain, and 88 for the Rurutu chain, for a total of 260 adjustable parameters for their age models.

Bono et al. (2019) estimated distance changes between the Hawaii and Louisville hotspots using pairs of approximately coeval volcanoes, i.e., separated by less than 3 Ma in age. They report modest nominal convergence (≈450 km) between the Hawaii and Louisville hotspot during the ≈30-Ma-interval of formation of the Emperor chain, but they emphasize the high rate of convergence during a short sub-interval of time.

Here we pursue an alternative approach by postulating that the uncertainty of seamount ages in the context of regional tectonics and plate motions may be much greater than the analytical uncertainty (Moore et al., 1987; Gripp & Gordon, 2002). We expect multiple tiers of uncertainty and variability in the age progression of any hotspot chain including the following: the within-flow uncertainty of an age date, the within-seamount uncertainty and variability of age dates, and the along-chain uncertainty and variability in age dates. Each tier may have uncertainties or variabilities that are considerably larger than that of lower tiers, as is typically observed, for example, in tiered paleomagnetic analysis (Irving, 1964; Cox & Gordon, 1984).

A typical hotspot volcano is formed over millions of years (Jackson et al., 1980; Heaton & Koppers, 2019); thus a precise age from a single dredge or drill sample may poorly represent the age of the bulk of a volcanic edifice, which is largely inaccessible to sampling. Furthermore, the Hawaiian chain consists of two lines of fractures (Dalrymple et al., 1973). Thus the local fracture propagation rate may influence volcano age. Pacific plate motion relative to the underlying plume may only be meaningfully estimated if averaged over many fracture segments. Instead of using the analytical uncertainty as the uncertainty in volcano ages for plate motion studies, we argue that an uncertainty accumulated over multiple tiers should be used as it likely better represents the probability that the plume was located under a seamount at its reported age. Herein the uncertainty along each hotspot track is estimated from the dispersion of the age dates about a hotspot age progression model having a limited number of adjustable parameters.

In our preferred analysis of the Hawaiian, Rurutu, and Louisville hotspot tracks for the past 80 Ma we use merely 30 adjustable parameters, 18 for the spatial fits and

12 for the fits to the age progressions. The latter number, 12, can be compared with the 260 adjustable parameters used by Konrad et al. (2018) to fit the age progressions for the three chains. With only 30 parameters for three chains, each with two subtracks, we and the readers have a good chance of understanding our model. Eighteen of the 30 adjustable parameters are fit to the spatial distribution of volcanoes (six adjustable parameters per track) and twelve of the adjustable are adjusted fit the 80 age dates available from the three chains. In contrast, we do not think it's possible to truly understand a model with hundreds of adjustable parameters. One expression of Occam's Razor is that "simpler hypotheses are better than complex ones", with which we strongly agree. A simpler hypothesis is easier to test and potentially falsify and thus make progress than is a complex hypothesis.

All three hotspot tracks examined herein are recognized as having an Eocene-age bend (i.e., a change in volcanic propagation direction). The Hawaiian-Emperor Bend (HEB) was recognized by Morgan (1972), who interpreted it as a record of a major change in the direction of Pacific-plate motion, an interpretation that was later challenged (Norton, 1995; Raymond et al., 2000; Tarduno et al., 2003, 2009; Hassan et al., 2016; Konrad et al., 2018; Heaton & Koppers, 2019). Morgan (1972) also proposed that analogous bends in the Macdonald and Easter Island hotspot tracks record the same change in Pacific plate motion. Watts et al. (1988) and Lonsdale (1988a) later established the significance of the Louisville chain, which is believed by many to contain the best record of a bend aside from the HEB (Wessel & Kroenke, 2008; Konrad et al., 2018; Wessel & Conrad, 2019). The Rurutu hotspot has been recently added to the list of Pacific hotspots that may have existed long enough to record a bend in the Eocene; plate motion models have been used to estimate the location of the Rurutu bend (RB) (Konrad et al., 2018; Finlayson et al., 2018).

Age dates from the Louisville track have been interpreted as indicating an age for the Louisville Bend (LB) of ≈51.2 Ma, which may be significantly older than the HEB (≈47.5–50 Ma (Sharp & Clague, 2006; O'Connor et al., 2013)). This age difference has led to the suggestion that the Eocene bends in Pacific hotspot tracks are asynchronous (Koppers & Staudigel, 2005; Koppers et al., 2011; Heaton & Koppers, 2019), which conflicts with hypotheses for bend formation that predict coeval bends, e.g., that the bends are the result of a change in Pacific plate absolute motion. To improve the resolution of the bend ages and their timing relative to other Eocene tectonic events including the collision of India with Eurasia (Rowley, 1996; Bouilhol et al., 2013) and the initiation of subduction of the Pacific plate in the west and southwest Pacific Ocean basin (Meffre et al., 2012; Arculus et al., 2015), herein we determine maximum likelihood estimates (and uncertainties) of the locations and ages of the bends of the Hawaii, Rurutu, and Louisville hotspot tracks. Moreover we consider the effect of the uncertainty in bend location on the estimate of bend age.

2 Data

For the Hawaiian-Emperor and Rurutu chains, we adopt the age dates of Konrad et al. (2018); for the Louisville chain, we adopt the age dates of Heaton and Koppers (2019). To supplement the locations of dated seamounts, we incorporate undated seamount locations along the Emperor and Louisville chains from the EarthRef seamount catalog (Koppers et al., 2010). Meiji Seamount from the Emperor chain was considered a geographic outlier and excluded from the data. Its exclusion, however, does not greatly alter our results. Table S5 contains relevant metadata plus a full list of the volcano ages and locations that served as input to our inversions.

3 Methods

3.1 Geographic Model

The analysis of age dates is separated from the spatial analysis of the hotspot tracks by building on procedures used in the determination of paleomagnetic Euler poles (Gordon et al., 1984; May & Butler, 1986). Each hotspot track is initially divided into two subtracks, one corresponding approximately to the age span of the Hawaiian chain and the other corresponding approximately to the age span of the Emperor chain. The volcano locations from both subtracks of a single track are inverted while requiring that the two subtracks meet at a unique point, which we take to be the bend in the track. For the Hawaiian-Emperor chain this point is the Hawaiian-Emperor Bend (HEB) and for the other two tracks, this point is a location analogous to the HEB; we refer to these other bends as the Louisville Bend (LB) and the Rurutu Bend (RB). We do not require that the bend coincides with the location of a seamount.

For a given trial location of a bend, by finding the best-fitting pole for each small circle from a trial-and-error grid-search, two best-fitting small circles are found, one for the Hawaiian-age subtrack and one for the Emperor-age subtrack. The radius of each small circle equals the distance between a trial bend location and the relevant trial pole location. Summed squared misfit, *SSM*, where $SSM = \sum_i \, (d_i - r_{\{h,e\}})^2$, d_i is the distance between the i^{th} seamount from a track and the trial pole for the relevant subtrack, and $r_{\{h,e\}}$ is the radius for the relevant subtrack trial pole (i.e., either the Hawaiian-age subtrack pole or the Emperor-age subtrack pole), is determined for each trial bend location and corresponding best-fitting small circle. The bend location for which the value of SSM is lowest is the maximum-likelihood estimate of the bend location. The standard deviation of the distance of seamounts about the relevant best-fitting small circle (i.e., either the Hawaiian-age small circle or the Emperor-age small circle) is given by $\sigma_{geo} = (SSM/\nu)^{1/2}$, where the number of degrees of freedom, ν, equals $N{-}n$, N is the number of seamounts (volcanoes) along a track, n=6 is the number of adjustable parameters needed to fit the bend and both small circles. Bend locations are searched at 0.1° resolution on a latitude-longitude grid. We complete each search for a best-fitting pole fit to a subtrack with a Nelder-Mead simplex algorithm to refine the parameter search beyond grid resolution and ensure the global minimum is found (Nelder & Mead, 1965; Press et al., 1986; J.-Y. Royer & Chang, 1991).

In the region surrounding the best-fitting bend location, sum-square normalized misfit (*SSNM*) is contoured to estimate the uncertainty of the location of the bend. To determine the normalized misfit, each misfit is divided by 33 km, which Wang et al. (2019a) determined to be the global mean of one-dimensional 1σ standard deviation in seamount location about the trend that best fits the neotectonic portions of many global hotspot tracks. The normalized misfits from a given subtrack are squared and then summed to obtain *SSNM*, i.e., $SSNM = \sum_i \, [(d_i - r_{\{h,e\}})/(33 \text{ km})]^2$. An increase of *SSNM* by $\sqrt{2}$ from $SSNM_{min}$, the minimum value of *SSNM*, defines the 1σ contour and an increase by $4 \times \sqrt{2}$ from $SSNM_{min}$ defines the 2σ contour where the factor $\sqrt{2}$ is incorporated so that the contours are appropriate for a two-dimensional, instead of a one-dimensional, σ (Cox & Gordon, 1984; Press et al., 1986).

Volcano locations are initially allocated to subtracks from prior estimates of the bend locations. For the Hawaiian-Emperor chain, we initially take Kimmei seamount as the youngest member of the Emperor subtrack and Yuryaku seamount as the oldest member of the Hawaiian subtrack (Sharp & Clague, 2006). This allocation is self-consistent in the sense that the resulting estimate of the HEB location essentially lies between the two seamounts. In contrast, for the Louisville chain, we initially take 169.0°W seamount as the youngest member of the Emperor-age subtrack and 168.3°W seamount as the oldest member of the Hawaiian-age subtrack. Results of initial inversions indicate, however, that the bend lies farther to the northwest. Thus we re-allocate the 169.0°W seamount to the Hawaiian-age subtrack, causing the 169.8°W seamount to become the youngest member of the Emperor-age subtrack, which results in a self-consistent allocation. For the Rurutu hotspot track, we allocate the Tuvalu chain and Gilbert Ridge to the Emperor subtrack and the Austral-Cook chain to the Hawaiian-age subtrack. Although, as discussed with the results below, the RB locates in the Tuvalu chain, we do not revise the grouping because of the large spatial gap between the Tuvalu and Austral-Cook chains.

The bend locations are also estimated using an alternative approach: The locations of seamounts along each subtrack are analyzed independently to determine the small circle that best fits in a least-squares sense. Each of the two small circles for a track are parameterized by the pole latitude, pole longitude, and small-circle radius, identically to how paleomagnetic Euler poles are determined (Gordon et al., 1984). With this approach we take the bend to be the intersection of the two small circles that occurs near the young end of the Emperor-age subtrack and the old end of the Hawaiian-age subtrack. The two methods of analysis gave identical locations for the bend and the poles and for the radii of the two small circles. That both approaches produce identical results and use the same number of adjustable parameters suggests that they are equivalent although parameterized differently.

Because of the huge uncertainty in the location of the RB, after initial analysis we assume that the RB is at the location proposed by Finlayson et al. (2018).

3.2 Age Model

The spatial analysis provides a foundation for the age analysis. The site locations for age dates are projected radially onto the small circle obtained for each subtrack of each chain. Distance along track is determined from the angle subtended about the pole that best fits the subtrack; angular distance is converted to surface distance in kilometers assuming a spherical Earth with a radius of 6371 km. Initially a two-parameter (slope and intercept) age model is fit by least squares to the equally weighted age dates projected along each subtrack. The significance of higher-order models is tested using the

F-ratio test of an additional term (Bevington, 1969). If the tests indicate that an additional term is significant, then the additional term (quadratic) term is incorporated.

The standard deviation of the age dates is determined from the dispersion of age dates about the best-fitting line or, if an additional term is significant, about the best-fitting straight-line plus quadratic term. The 1σ uncertainty in age dates is taken to equal this standard deviation. We linearly propagate the 1σ uncertainty in age dates to estimate the 1σ uncertainty in estimated parameters including the age of the bends (Bevington, 1969).

Because bend ages extrapolated from each subtrack age progression generally differ from one another, we instead seek the maximum likelihood estimate of bend age by using Lagrange multipliers to constrain the age models of both subtracks to agree at the chain bend (Boas, 2006). This unique bend age is determined via a one-dimensional numerical search through possible ages of the maximum likelihood location of the bend found from geography alone. The value of age at which the SSNM increases by 1 above the minimum value of SSNM is taken to be the 1σ uncertainty limit and the value at which it increases by 4 is taken to be the 2σ uncertainty limit (Press et al., 1986).

Geographic uncertainty in the bend age is incorporated by estimating the geographic one-dimensional 1σ of the bend location in the direction parallel to each subtrack. This geographic uncertainty is mapped into age uncertainty by dividing it by the absolute value of the best-fitting volcano-age-progression rate near the bend; the resulting variance is added to the variance in ages.

An assumed-coeval age for the HEB and LB is determined using a weighted mean of the separately estimated ages of each. Rurutu is omitted due to the huge uncertainty of its bend age and location. For our preferred age model, in which the chains bend coevally, in principle the location of the HEB and LB would both be allowed to adjust within uncertainty to better attain coevality. The location of the HEB is so much better constrained than that of the LB, however, that we left the former unchanged and only allowed the LB location to adjust.

3.3 Inter-Hotspot Distance

Inter-hotspot distance as a function of age is determined from the great-circle distance between coeval age-model locations along two different tracks while approximating the Earth as a sphere. The uncertainty in inter-hotspot distance is estimated for each coeval pair of locations from their uncertainty in location. The across-track component of location uncertainty is determined from the across-track dispersion of volcano locations (Wang et al., 2019a). The along-track uncertainty is determined by linear propagation of the age model uncertainty into distance uncertainty by multiplying by the absolute value of the local volcanic propagation rate. The uncertainty in inter-hotspot distance is found by summing the variances along the great circle connecting each pair of coeval locations.

3.4 Plate-Hotspot Reconstructions

The motion of the Pacific plate relative to the three hotspots since 80 Ma is determined at 1-Ma intervals from the geographic and age models using the N-hotspot method of Andrews et al. (2006). This maximum-likelihood method permits an arbitrary number of hotspot tracks having elliptical location uncertainties to be fitted. Rurutu is excluded from the reconstructions between 10 Ma and 50 Ma. The larger of the (1) observed one-dimensional 1σ standard deviation of seamount locations along a track or (2) the global one-dimensional 1σ standard deviation value of 33 km found by Wang et al. (2019a) is adopted as the input uncertainty.

3.5 Nominal Plume Drift Relative to Absolute Reference Frame

If the effect of estimated plate motion is subtracted from an age model, the implied nominal hotspot or plume motion relative to the underlying reference frame is obtained (Wessel & Conrad, 2019). The underlying absolute reference frames herein are taken to be either a mean mantle reference frame or a mean hotspot reference frame.

4 Results

Figure 1 shows the spatial best-fitting models. Table S1 reports the best-fitting spatial parameters, spatial standard deviation, and numbers of degrees of freedom. Figure 2 shows the best-fitting age models assuming coeval bend ages; age models not assum-

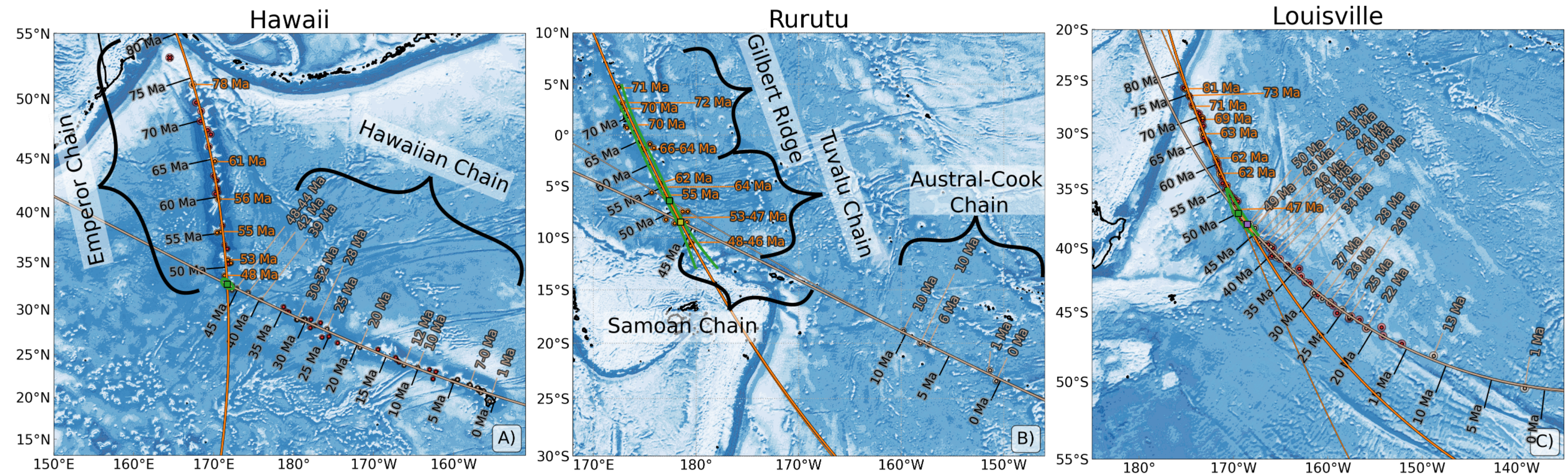

Figure 1. Spatial fits to the Hawaiian, Rurutu, and Louisville hotspot tracks. Best-fit small circles to both the Hawaiian-age (tan) and Emperor-age (orange) subtracks are shown atop the gravity grid of Sandwell et al. (2014). Orange-filled and tan-filled circles are dated seamounts assigned respectively to the Emperor-aged and Hawaiian-aged subtrack; the red-filled circles are undated seamounts. Orange and tan numerals and text are the nominal ages of the dated seamounts; black numerals are ages from the age-progression model for assumed-coeval Eocene age bends in all three chains. Crosses indicate seamounts excluded from analysis. Green-filled squares indicate maximum likelihood bend locations inverted from the two subtracks; green contours show the corresponding two-dimensional 2σ uncertainty limits. Yellow-filled square on the Rurutu track shows the bend location reported by Finlayson et al. (2018) for the location of the Rurutu Bend. The purple-filled square in 1C is the location of the Louisville Bend in our preferred model for which we assume the bend is coeval with the Hawaiian-Emperor Bend. The thinner small circles shown in 1B and 1C show the original maximum likelihood small circles from the model without coeval bends.

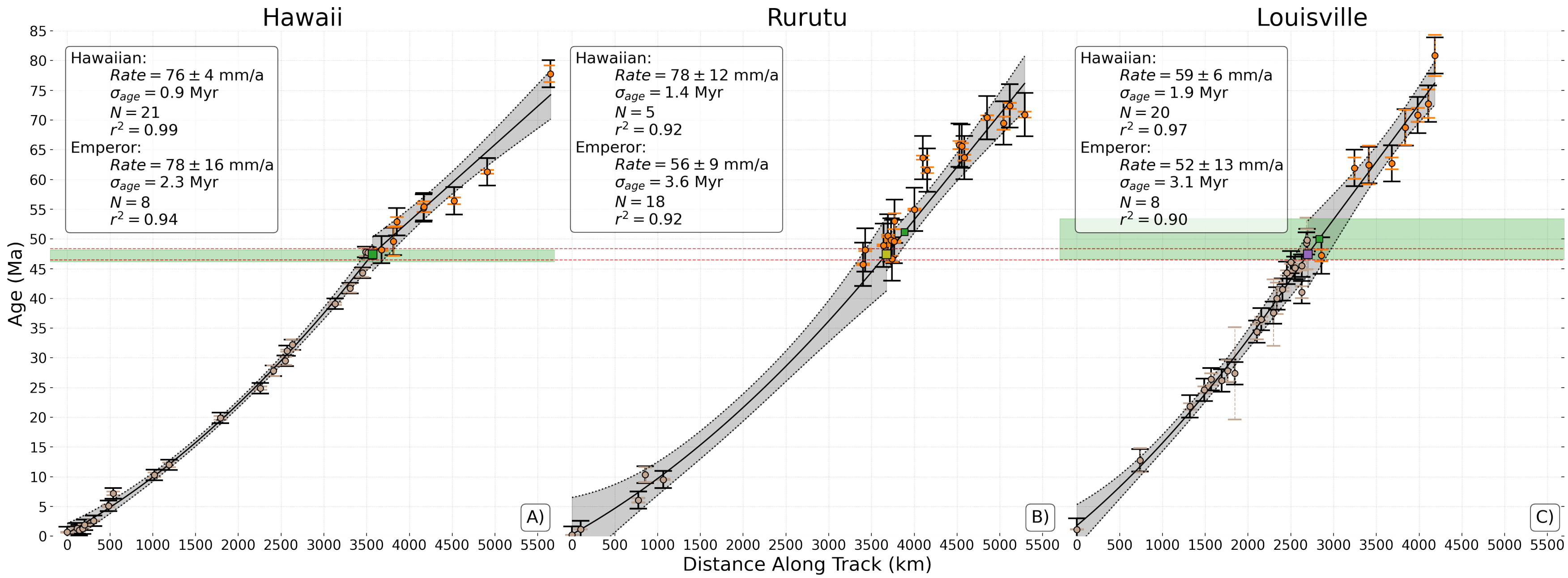

Figure 2. Hotspot age versus distance for the model assuming coeval bend ages; solid orange and tan error bars are the reported analytical $\pm 2\sigma$ uncertainties in seamount age, dotted orange error bars are the reported ages spanned by seamounts with more than one age date (Table 2 of Heaton and Koppers (2019)), and black error bars show the seamount age uncertainty inferred from the dispersion of the age dates. Green squares show the maximum likelihood location and age of the bends in each chain. Yellow square shows the RB location determined by Finlayson et al. (2018) using absolute plate motion models; purple square shows the LB location implied by the age models if coevality with the HEB is assumed. Red dashed lines indicated the uncertainty in the coeval bend age. Green shaded region on 2A and 2C show the uncertainty in the independently determined Hawaiian and Louisville bend ages. Rates given for the quadratic models of the Hawaiian subtrack are the mean rate over Hawaiian time (0–47.4 Ma). Quoted uncertainties on volcanic propagation rate are $\pm 2\sigma$

.

ing coeval bend ages are shown in Figure S1. The best fit parameters of the age models and their covariance matrices can be found in Tables S3–S4. The estimated bend locations and uncertainties per track are shown in Figures 3a–c and listed in Table S1.

F-ratio tests for the significance of adding a quadratic term to the fit of age versus distance for the Hawaiian-age subtracks result in p=3.5 $\times$ 10^{-7} for Hawaii, 0.88 for Rurutu, and 0.01 for Louisville; for the Emperor-age subtracks, p =0.09 for Emperor, 0.04 for Rurutu, and 0.99 for Louisville. F-ratio tests for a cubic term for Hawaiian-age subtracks resulted in p=0.10 for Hawaii, 0.24 for Louisville, and 0.83 for Rurutu. The only age dates from subaerial samples in our analysis are from the Hawaiian chain and they indicate a significantly higher propagation rate (p=2 $\times$ 10^{-5}) and have a lower σ_{age} (≈0.7 Ma) than age dates from Hawaiian-chain submarine samples. Incorporation of the subaerial Hawaiian-chain age dates results in a significant F-test for the addition of a quadratic term. Table S2 presents test statistics, SSM values, and degrees of freedom for these calculations.

From the Hawaiian-age subtracks, we estimated an age of 47.6±1.3 Ma for the HEB, an age of 30.0 Ma for the RB, and an age of 50.9±3.8 Ma for the LB. From the Emperor-age subtracks, we estimated an age of 46.7±1.4 Ma for the HEB, an age of 50.6 Ma for the RB, and an age of 48.9±3.2 Ma for the LB. When the two subtracks of each chain are constrained to agree in age at its bend, the bend ages are 47.2±1.0 Ma for the HEB, 50.6 Ma for the RB, and 50.3±3.4 Ma for the LB (Figures 1–3 and Figure S4). No useful age uncertainty could be estimated for the RB because its geographic uncertainty is huge. If the HEB and the LB are constrained to be coeval, the maximum likelihood bend age is 47.4±1.0 Ma.

Inter-hotspot distances as a function of age are shown in Figures 3d–e. When the bends are not constrained to be coeval, the change in distance between the Hawaiian and Louisville hotspots over the past 80 Ma has been ≈910±930 km. The change in distance over the past 72 Ma between the Hawaii and Rurutu hotspots and between the Louisville and Rurutu hotspots respectively were ≈330±600 km and ≈450±1140 (Figure 3d). If divided by the relevant time intervals, these correspond to mean nominal rates of motion between hotspot pairs of −11 mm/a (Hawaii-Louisville), −5 mm/a (Hawaii-Rurutu) and −6 mm/a (Rurutu-Louisville), where negative values indicate the distance is decreasing with time; all quoted rates differ insignificantly from zero.

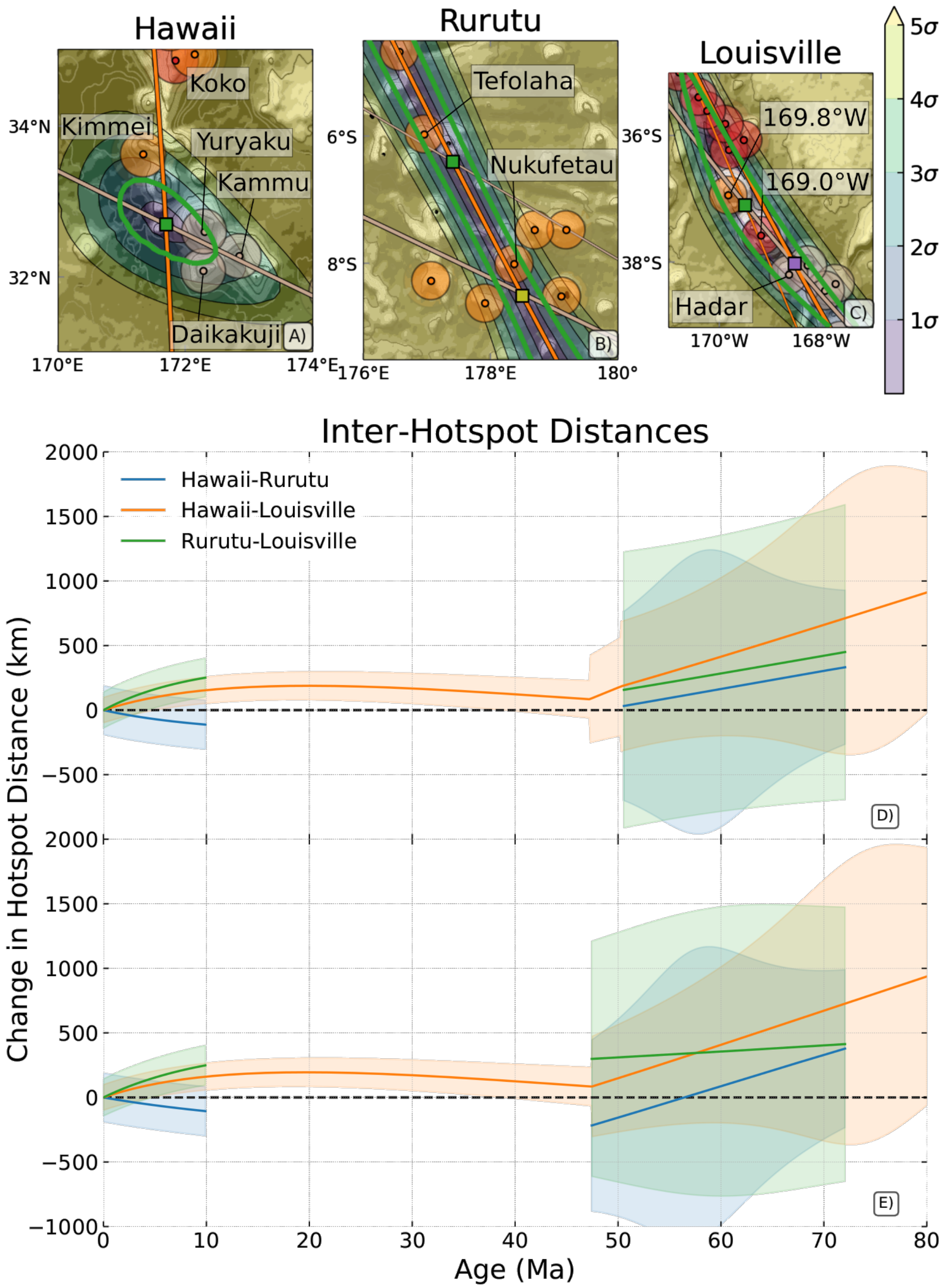

Hawaii
Rurutu
Louisville
Koko
Kimmei
Yuryaku
Kammu
Daikakuji
A)
34°N
32°N
170°E
172°E
174°E
Tefolaha
Nukufetau
B)
6°S
8°S
176°E
178°E
180°
169.8°W
169.0°W
Hadar
C)
36°S
38°S
170°W
168°W
5σ
4σ
3σ
2σ
1σ
Inter-Hotspot Distances
Hawaii-Rurutu
Hawaii-Louisville
Rurutu-Louisville
Change in Hotspot Distance (km)
Age (Ma)
D)
E)

Figure 3. Bend locations and inter-hotspot distances over time for the Hawaii, Rurutu, and Louisville hotspot tracks. The green-filled squares show the maximum likelihood estimates of the bend location for each chain. Tiny tan-filled circles are dated seamount locations along a Hawaiian-age subtrack. Tiny orange-filled circles are dated seamount locations that lie along an Emperor-age subtrack. Tiny red-filled circles are undated seamount locations. Larger color-filled circles centered on seamount locations have a radius of 33 km (equals one-dimensional 1σ). Each best fit subtrack is shown by an orange or tan small circle segment (the thinner small circle segments on 3B and 3C show the maximum likelihood best fitting small circles). Underlying contour, gravity grid (Sandwell et al., 2014). Overlying contour, chi-squared surface for the bend location contoured in increments of two-dimensional 1σ up to 5σ; 2σ contour is green. The label"169.0°W" indicates a location midway between the 169.3°W and 169.0°W volcanoes, which are joined at depth. 2D shows inter-hotspot distance (with shaded $\pm 2\sigma$ uncertainties) versus age for case in which the bends are not forced to be coeval. Hawaiian-age subtrack distance between Rurutu and other hotspots is only shown from 0 to 10 Ma. 2E is the same as part D but when the bends are assumed coeval.

If the bends are constrained to be coeval, the total change in distance between these hotspot pairs is $\approx 940 \pm 1000$ km, $\approx 380 \pm 600$ km, and $\approx 420 \pm 1060$ km respectively for the Hawaii-Louisville, Hawaii-Rurutu, and Rurutu-Louisville hotspot pairs (Figure 3e). If divided by the relevant time intervals, these correspond to mean nominal rates of motion between hotspot pairs of -12 mm/a (Hawaii-Louisville), -5 mm/a (Hawaii-Rurutu) and -6 mm/a (Rurutu-Louisville), all also differing insignificantly from zero.

For Hawaiian time (i.e., the past ≈ 48 Ma), if the bends are not constrained to be coeval, and with a quadratic fit, the Hawaii and Louisville hotspots first nominally move farther apart and then nominally move closer together; the net effect is little or no motion between the two hotspots (Figures 3d–e). The net change in distance between these two hotspots during all of Hawaiian time is $\approx 90 \pm 140$ km (Figure 3d). The implied mean rate of motion between the Hawaii and Louisville hotspots averaged over the past 48 Ma is -2 ± 4 mm/a. For the 10-Ma interval containing age dates along the Cook-Austral chain, the rates of motion between Hawaii-Rurutu and Rurutu-Louisville respectively are 11 ± 26 mm/a and -25 ± 26 mm/a. If the bends are instead constrained to be coeval, the net change in distance between Hawaii and Louisville also is $\approx 90 \pm 140$ km (Figure 3e) and the rates

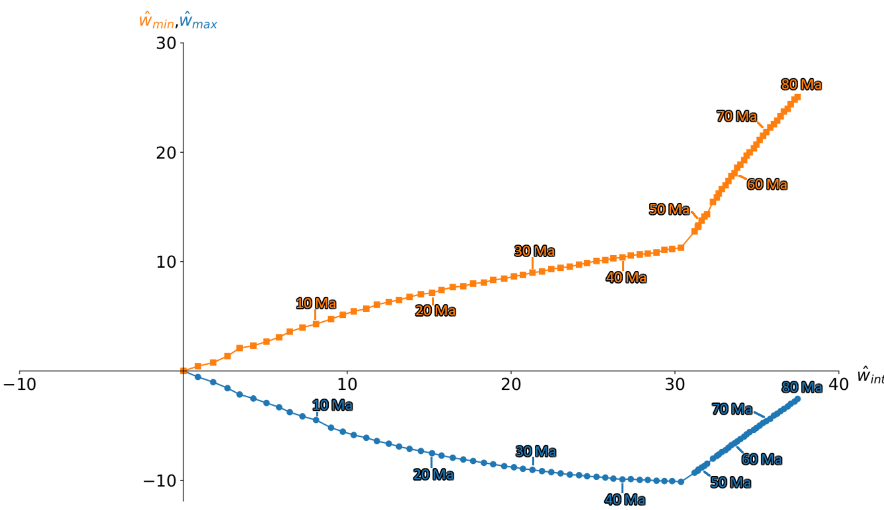

Figure 4. Vector end point diagram in units of degrees (of angle of rotation) of our Pacific plate-hotspot finite rotations at 1 Ma intervals between 80 and 0 Ma projected onto the eigenvectors of the covariance matrix for the 11 Ma rotation. Modest curvature between 80 and 48 Ma indicates a gradual change in orientation of the rotation. A sharp change in orientation of plate rotation occurs between 48 Ma and 47 Ma, consistent with our treatment of a coeval bend in the chains at that age. A gradual change in orientation is indicated over the most recent 47 Ma with the most rapid, but still gradual, change occurring ≈20–10 Ma.

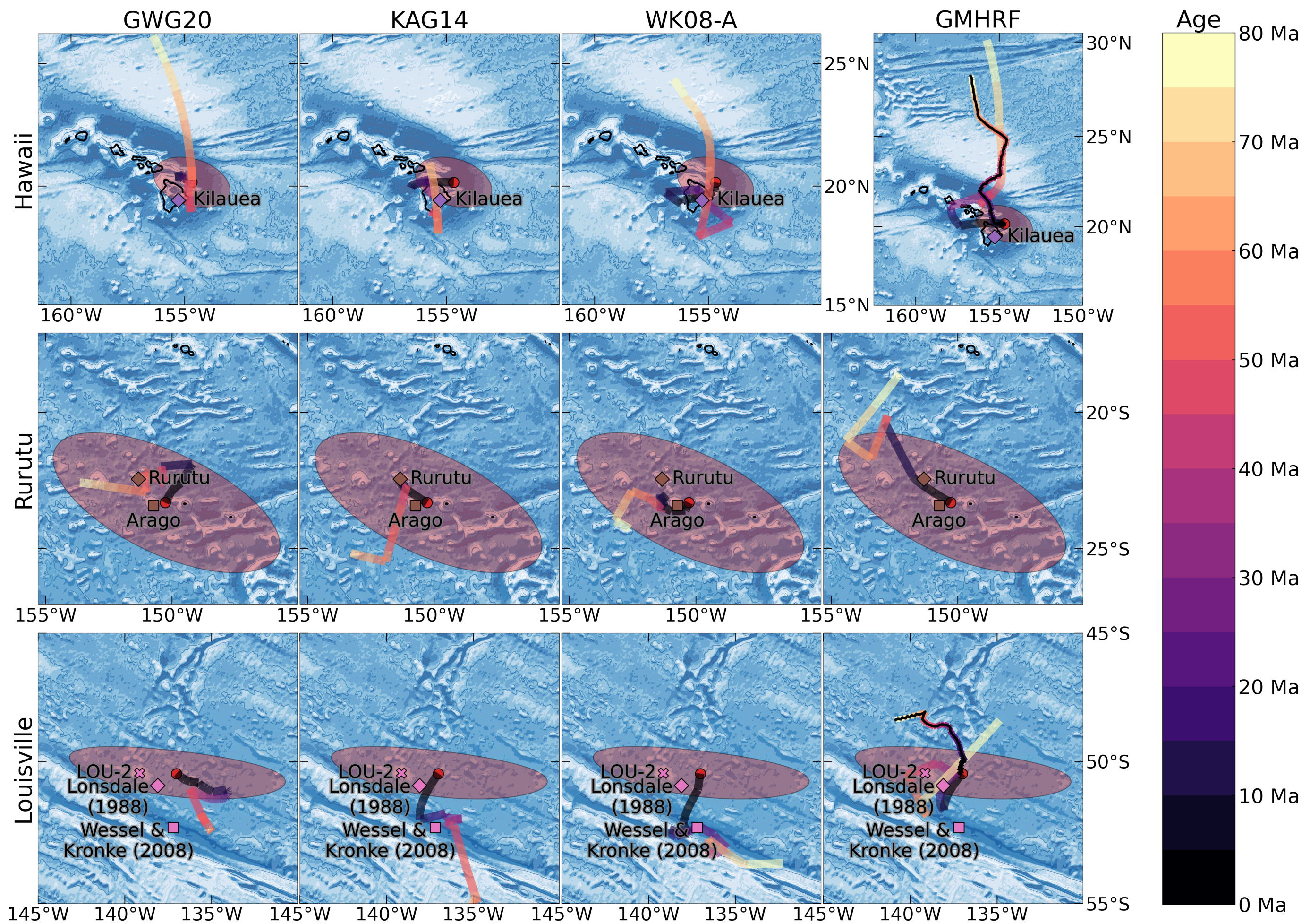

Figure 5. Nominal misfit to our preferred (coeval-bend) age models implied by the Pacific plate absolute rotations of: GWG20 (This study), KAG14 (Koivisto et al., 2014), WK08-A (Wessel & Kroenke, 2008), and the GMHRF (Doubrovine et al., 2012). None of the misfits are significant. For plate rotations relative to assumed-fixed hotspots, this misfit is the nominal motion implied for each hotspot. For the GMHRF it is the misfit between the age models and the motion of hotspots predicted by Doubrovine et al. (2012). Red-filled circle and uncertainty ellipse mark the current hotspot location from our age models. Black centered line for the GMHRF is the hotspot motion predicted by Doubrovine et al. (2012). For KAG14, the oldest reconstruction of which is 67.7 Ma, we only show nominal hotspot motion from that oldest reconstruction to present.

also are the same, i.e., -2 ± 4 mm/a, 11 ± 26 mm/a, and -25 ± 26 mm/a respectively for the Hawaii-Louisville, Hawaii-Rurutu, and Rurutu-Louisville hotspot pairs.

For Emperor time (i.e., 80–48 Ma), if the bends are not constrained to be coeval, the change in distance between Hawaii and Louisville is 830±940 km; the mean relative motion rates are −24±36, −14±44, and −14±52 respectively for Hawaii to Louisville, Hawaii to Rurutu, and Louisville to Rurutu. If the bends are instead constrained to be coeval, the change in distance between Hawaii and Louisville is 850±1010 km; the mean rates respectively are −26±34 mm/a, −24±38 mm/a, and −5±46 mm/a for the Hawaii-Louisville, Hawaii-Rurutu, and Rurutu-Louisville hotspot pairs.

The sequence of finite rotations that we determine from these age models are illustrated in Figure 4 and listed in Table S6. Misfits of the three preferred hotspot age models relative to various proposed absolute frames of reference are illustrated in Figures 5 and S5.

5 Discussion

5.1 Spatial Fit to Hotspot Tracks

The Hawaii and Louisville tracks are well represented by our simply parameterized models. The Rurutu track is well represented from 0 to 10 Ma and from 50 to 80 Ma (Figures 1 and 3). The 35-km value of σ_{geo} for the Hawaii hotspot track (Table S1) is similar to the 33-km value for the mean σ_{geo} for the young portions of 15 globally distributed hotspot tracks (Wang et al., 2019a). In contrast, the 20 km value of σ_{geo} for the Louisville track is small and the 72 km value of σ_{geo} for the Rurutu track is large. These variations in σ_{geo} may reflect a real difference in the widths of the the tracks of the three hotspots. Alternatively, they may be caused respectively by incompleteness of our catalog of Louisville volcano locations (e.g., volcanoes evident on Figures 1c and 3c but not included in the quantitative analysis) and by the inclusion of volcanoes in the Rurutu track that may not have been produced by the Rurutu hotspot.

5.2 Locations of the Bend in Each Track

Prior work placed the HEB either at Kimmei seamount (near the southern end of the Emperor subtrack) or at one of the three seamounts (Daikakuji, Yuryaku, or North Kammu seamount) near the western end of the Hawaiian subtrack (Dalrymple & Clague, 1976; Sharp & Clague, 2006; O'Connor et al., 2013) (Figure 3a). The maximum-likelihood HEB location (Table S1, Figures 1a and 3a), which we do not require to coincide with the location of a volcanic edifice, lies south-southeast of Kimmei seamount and west-northwest of Yuryaku seamount. The two-dimensional 2σ contour for the HEB location includes the point location of only one seamount, Yuryaku.

The RB determined from the small circles fit to the two Rurutu subtracks lies in the Tuvalu chain, near Tefolaha seamount, north of Nukufetau seamount where Finlayson et al. (2018) estimated the bend to be located (Table S1, Figures 1b and 3b). Thus the trend of the Hawaiian-age subtrack of Rurutu may be too poorly resolved to reliably locate the bend. Alternatively, some seamounts from the Tuvalu chain may not be products of the Rurutu hotspot.

Ideas about a possible bend location in the Louisville chain have evolved over time with suggestions including a kink near 166°W (Hayes & Ewing, 1971), a kink at 167.5°W (Epp, 1978), a break in trend near 37.5°S (corresponding to a longitude near 169°W) (Watts et al., 1988), and a bend location just east of a double peaked guyot, the 169.3/169.0°W guyot (Lonsdale, 1988a). Following Watts et al. (1988) and (Lonsdale, 1988a), Koppers et al. (2011) and Heaton and Koppers (2019) take the bend to lie at 169°W. While our analysis indicates that the LB location is well-constrained in the across-track direction, it is poorly constrained by the chain geometry in the the along-track direction (Figures 1C and 3C). The maximum likelihood location is 37.1°S, 169.5°W, a modest distance northwest of prior estimates. The two-dimensional 2σ uncertainty region about the maximum likelihood bend location includes eight of the point locations for the volcanoes, including the 169.8°W, 169.3/169.0°W, and Hadar guyots. Several other volcanoes lie partly in the uncertainty region. As discussed further below, when constrained to be coeval with the HEB, the LB is best located at 38°S, 168.5°W, near Hadar Guyot (Table S1, Figures 1c and 3c), between the locations suggested by Epp (1978) and by Lonsdale (1988a).

5.3 Fit to Age Dates Along Hotspot Tracks

When the bends are not constrained to be coeval, the dispersion of age dates along the three chains is lower for the younger (Hawaiian-age) subtracks (σ_{age} = 0.9 Ma, 1.6 Ma, and 1.9 Ma respectively for the Hawaii, Rurutu, and Louisville tracks) than for the older (Emperor-age) subtracks (σ_{age} = 2.5 Ma, 2.8 Ma, and 3.2 Ma) (Figure S1). The coeval-bend age model gives similar results (Figure 2). Values of σ_{age} are an order of magnitude larger than the analytical uncertainties ($\sim$0.2 Ma), which suggests that the latter are unrealistically small in the context of volcanic propagation rates on time scales of tens of millions of year. The misfits of the age dates herein are not dissimilar to the 2 Ma to 4 Ma misfits found by Wessel and Conrad (2019).

For each of the three tracks, the best-fitting volcanic propagation rate differs insignificantly between its two subtracks (Figure 2). The Hawaiian-age subtrack of the Louisville track also indicates a significant speed up during Hawaiian time, which is consistent with the results of Andrews et al. (2006), who found an $\approx$ 50% increase in propagation rate along the Hawaiian chain near $\approx$25 Ma with an additional smaller increase near $\approx$6 Ma. The use of a quadratic term in our Hawaiian-subtrack age models results in one more adjustable parameter (per chain) than for a linear fit. We neglect the subtle change in trend between neotectonic Pacific plate motion relative to the hotspots and that averaged over Hawaiian time (i.e., past $\approx$48 Ma) (Cox & Engebretson, 1985; Pollitz, 1986; Andrews et al., 2006; Austermann et al., 2011; O'Connor et al., 2013; DeMets & Merkouriev, 2016; Wang et al., 2019a).

Including a quadratic term does not significantly improve the age progression fit for the Emperor-age subtracks except for a possible slow down in the Rurutu track around 70 Ma, which indicates a near reversal in direction of volcanic propagation in the Rurutu track. A reversal seems far-fetched (Konrad et al., 2018). Thus we do not model a change in hotspot propagation speed during Emperor time.

5.4 Age of the Bends in Pacific Hotspot Chains

An early estimate of the age of the HEB, from the ages of formation of the boundary seamounts Daikakuji, Kimmei, Yuryaku, and Koko (Dalrymple & Clague, 1976), was 42±1.4 Ma. Newer ages for Daikakuji and an interpolated age for Kimmei seamount (Sharp & Clague, 2006), estimated using modern geochronological techniques, indicated an age range of 50–47 Ma. O'Connor et al. (2013) arrived at a similar 50 Ma upper bound on the age of the HEB, but suggest that the sharpest point of the HEB near Daikakuji and Yuryaku seamount is best dated as 47.5 Ma. Our estimate of 47.2±1.0 Ma for the unique age of the HEB differs insignificantly from the 47.5 Ma age estimated for the sharpest point of the HEB, while being younger than the 50-Ma upper bound.

Watts et al. (1988) estimated the age of the LB as ≈43 Ma based on a linear fit to all age data available at the time. Lonsdale (1988a) estimated the 169.0/169.3°W seamount, which he suggests is the seamount nearest the LB, as being ≈45-44 Ma. Similar to the HEB, the LB was later redated using ^{40}Ar/^{39}Ar methods and an age of ≈51–50 Ma was estimated assuming the LB lies at 169°W (Koppers et al., 2011). The most recent estimate for the age of the LB (assumed to lie at 169°W) is 51.2 Ma, which suggests that the LB is ≈4 Ma older than the HEB (Heaton & Koppers, 2019). If true, the bends would be asynchronous and therefore unlikely to share a common formation mechanism, such as a change in plate motion.

Our results indicate otherwise, however. Unlike prior studies, we explicitly consider quantitative estimates of the uncertainty in the location of the LB. The two-dimensional 2σ limits extend over a distance exceeding 500 km, from 34.9°S to 39.0°S and from 170.8°W to 167.8°W (Figures 1c and 3c), which spans an age range of ≈10 Ma (Figure 2). When the appropriate uncertainty in age induced by the uncertainty in LB location is included, the difference in the ages of the maximum likelihood bend locations (when not constrained to be coeval) is an insignificant 3.1±3.5 Ma (Figure S4).

Thus the full uncertainty in LB age precludes the exclusion of coeval bend ages. Therefore we cannot exclude the hypothesis that the formation of the bends have a common tectonic cause, in particular a change in Pacific plate absolute motion near ≈47 Ma. Mainly because the location of the HEB is better constrained than that of the LB, the best estimate for an assumed-coeval bend age, 47.4±1.0 Ma, is closer to the estimated HEB age than to the estimated LB age. Our preferred model thus is the one in which we constrain the bends to be coeval. As discussed above, the resulting preferred location of the LB is at 38°S, 168.5°W (Table S1, Figures 1C and 3C). Within uncertainty, at 47.4±1.0 Ma the assumed-coeval bend age is indistinguishable from the age of the C21o geomagnetic reversal, dated as 47.3 Ma (Gradstein et al., 2012) or 47.8 Ma (Westerhold et al., 2018).

5.5 Evolution of Inter-Hotspot Distance

Our results indicate no significant motion between three key Pacific hotspots over the past ≈80 Ma. Rates of inter-hotspot motion are best constrained between the Hawaii and Louisville hotspots at merely −2±4 mm/a for the past 48 Ma and −24±36 mm/a for 80 to 48 Ma. If the bounds found for the past 48 Ma are typical of global rates of motion between hotspots over long intervals of geologic time, the fixed hotspot approximation is undoubtedly excellent. If, however, global rates of motion between hotspots have been near our 80–40 Ma upper bound of ≈60 mm/a over long intervals of time then the fixed hotspot approximation would not be useful except over the past ≈48 Ma. That rates of motion over the past 48 Ma between hotspots in different ocean basins are low (Koivisto et al., 2014) supports the global usefulness of the fixed hotspot approximation. Investigations that show that rates of global inter-hotspot motion over neotectonic time are low give further support for the usefulness of the fixed hotspot approximation (Morgan & Morgan, 2007; Wang et al., 2017, 2019a). Thus there is strong evidence for the usefulness of the fixed hotspot approximation over the past 48 Ma.

What about further back in time? Pre-48 Ma plate reconstructions are less robust. Unknowns and uncertainties abound. A rational approach is to assume that the fixed hotspot approximation is valid for the Earth before 48 Ma and to continue to test this assumption rigorously, leaving open the possibility that hotspots and their presumed underlying mantle plumes—although approximately fixed for the past 48 Ma—moved rapidly over time intervals preceding ≈48 Ma. Our results herein do not exclude the possibility of rapid motion (with an upper limit near 60 mm/a) but also do not exclude the possibility of approximately fixed hotspots (with a lower limit of zero). Some prior studies claim proof of rapid motion between hotspots before 48 Ma. We think that these claims are premature. Here we consider two recent studies: (1) Konrad et al. (2018), and (2) Bono et al. (2019).

Konrad et al. (2018) estimated inter-hotspot rates of motion for the interval 60 to 48 Ma of -53 ± 42 mm/a, -57 ± 54 mm/a, and zero respectively for the Hawaii-Louisville, Hawaii-Rurutu, and Louisville-Rurutu hotspot pairs. Their first two rates tend to be higher, and all their uncertainties tend to be larger, than ours because of the higher number of adjustable parameters and the smaller age window they employed compared with ours. Their nominal rates are within the uncertainties we find before 48 Ma, but our upper limits are much lower than theirs. Within uncertainty, our rates include zero and theirs nearly do so. Therefore neither their results nor ours require rapid motion between hotspots; both are consistent with low rates of motion between hotspots. Many more age dates are needed before the uncertainties can be shrunk enough to distinguish between wildly different conjectures concerning rates of inter-hotspot motion. For example, age dates from the Emperor chain, spanning ≈80–48 Ma, are sparse, with only eight total, six of which give values of 56.1 Ma or less (Figure 2A); thus a 24-Ma interval (from ≈80 Ma to 56 Ma) of its ≈32-Ma-long chain history is sampled by only two age dates. While the Louisville chain is well sampled near, and a little younger than, the age of the LB and between 81 and 62 Ma (with 7 age dates), there are no age dates for the 12-Ma-long interval between 62 Ma and 50 Ma, representing more than one-third of Emperor-age time.

Bono et al. (2019) claim that "...A dramatic decrease in distance between Hawaiian-Emperor and Louisville chain seamounts between 63 and 52 Ma confirms a high rate of southward Hawaiian hotspot drift (∼47 mm/a)....". We assert that their results are inconsistent with the hypothesis they claim to be testing. Instead, the change in distance they find between the Hawaii and Louisville hotspots is much smaller than predicted by their proposal of ≈1500 km of southward motion of the Hawiian hotspot through the mantle during an ≈30-Ma-long interval (i.e., from ≈80 and 50 Ma when the Emperor chain was created as illustrated in their Figure 3a). If the Hawaii hotspot moved purely southward by 1500 km and if the Louisville hotspot was approximately fixed, the Hawaiian hotspot and Louisville hotspot should have converged by nearly 1500 km between ≈80 and 50 Ma. Their results (as shown in Figure 3b of Bono et al. (2019)) indicate that the hotspots nominally converged by merely 450 km over the relevant 30-Ma-long time interval, much closer to zero motion than to the predicted 1500 km. Their analysis also indicates effectively no motion between the two hotspots between ≈80 and 60 Ma—for nearly two-thirds of the age span of the Emperor chain there was no discernible motion between the two hotspots. Thus, by their results, most of the chain formed while the Hawaiian hotspot was fixed relative to the Louisville hotspot, contradicting their hypothesis for the origin of the Emperor chain.

We estimate the nominal convergence between Hawaii and Louisville from 80 to 48 Ma to have been ≈850 km, nearly twice the nominal value found by Bono et al. (2019) and 55% larger than the nominal value found by Wessel and Kroenke (2009). Our upper limit (i.e., including uncertainty) on motion during Emperor time is 1860 km and our lower limit is zero, which follow from uncertainties much larger than estimated by Wessel and Kroenke (2009). With currently available data constraining the relative motion between the Hawaii and Louisville hotspots, therefore, we can neither reject the hypothesis of 1500 km of southward motion of Hawaii through the mantle nor reject the hypothesis of fixed hotspots. Our analysis is likely to be more reliable than that of Bono et al. (2019) as we use all 57 age dates from the two chains and estimate merely 12 adjustable parameters leaving 35 degrees of freedom. In contrast, Bono et al. (2019) use only 16 age dates, discarding the information in the other 41 age dates, and then estimate eight parameters (distances), leaving merely eight degrees of freedom.

5.6 Hypothesized Motion of the Hawaiian Hotspot Relative to the Mantle

Substantial prior work has focused on the motion of the Hawaiian hotspot relative to the spin axis and noted a southward shift in hotspot location (Kono, 1980; Gordon & Cape, 1981; Acton & Gordon, 1991; Petronotis et al., 1994). An important hypothesis considered in this early work is that the southward motion is part of a global re-orientation of Earth with respect to the spin axis termed true polar wader (Morgan, 1981; Gordon & Cape, 1981). In particular, the results and analysis of Petronotis et al. (1994) are consistent with the hypothesis that true polar wander occurred near or just prior to the formation of the HEB. Later work has focused on an alternative hypothesis, that the observed latitudinal shift of the hotspot is instead due to its southward motion through the mantle. This latter interpretation further proposes that the HEB does not record a change in direction of plate motion, but instead was caused by the cessation of southward motion of the Hawaiian hotspot through the mantle while the angular velocity of the Pacific plate remained unchanged (Tarduno et al., 2003). Our current investigation directly informs us neither about changes in hotspot location relative to the spin axis nor about Hawaii's hypothesized motion relative to the mantle, but only about the relative motion between Pacific hotspots. Nonetheless our new results provide information that may exclude some hypotheses.

In our test of the hypothesis of Bono et al. (2019), we assumed that the Rurutu hotspot and the Louisville hotspot were fixed in the mantle. Moreover, we took the predicted southward motion of Bono et al. (2019) to be motion in a purely southward direction. Prior workers have noted, however, inconsistencies that arise for purely southward motion.

First, using a simple vector analysis and a Pacific plate-hotspot speed of 62 mma/a during formation of the Emperor chain, Sager (2007) (and later Torsvik et al. (2017)) showed that the Hawaiian hotspot was required to have a westward component of motion roughly equal to its southward component of motion if no change in Pacific plate motion occurred at the time of formation of the HEB. The westward motion is required for the Hawaiian hotspot to reproduce the geometry of the Emperor chain while the Pacific plate moved with an angular velocity similar to its average over the past 48 Ma. Sager (2007) argued that this was inconsistent with geodynamic models that indicated that the Hawaiian hotspot should have been moving to the south or southeast. With respect to the analysis presented herein, the addition of a westward component of motion alters the predicted distance change relative to an assumed fixed Louisville hotspot. Much less change in distance is predicted than for purely southward motion of the Hawaii hotspot; thus southwest, instead of purely south, motion is a better fit to the nominal distance change we find between the Hawaii and Louisville hotspots.

Second, Torsvik et al. (2017) expanded on these arguments and showed that if the Hawaiian hotspot had moved purely south while Pacific plate motion had remained unchanged, the rate of southward motion would have had to have been a whopping ≈420 mm/a, which is clearly excluded by our new results. Torsvik et al. (2017) reject this scenario as it requires the entire Emperor chain to have formed in 5 Ma. We concur.

Third, Torsvik et al. (2017) considered another scenario with slower (64 mm/a), but still purely south, motion of the Hawaiian hotspot. In this case, fitting the Emperor chain geometry requires sluggish Pacific plate motion before 47 Ma, but dramatically faster motion after. In this scenario, the Hawaiian hotspot moved southward for 33 Ma for a displacement of ≈2120 km. Torsvik et al. (2017) dismissed this scenario as not being supported by any models or observations. Here we reject it because it predicts 2070 km of convergence between the Hawaiian hotspot and a fixed Louisville hotspot, which exceeds the the 850 ±1010 km change in distance that we determined above.

Sager (2007) and Torsvik et al. (2017) may be premature, however, in rejecting models with significant westward components of motion. Their rationale is that geodynamic models predict motion to the south to southeast rather than to the southwest or west-southwest. Some of these geodynamic models attempt to improve on the fixed hotspot approximation with predictions of how hotspots have moved over geologic time (e.g., the GMHRF of Doubrovine et al. (2012), mentioned above). Recently, however, Wang et al. (2019b) showed that the GMHRF fits neotectonic trends of hotspot tracks much worse than they are fit by assuming fixed hotspots. They conclude that "...Either plume conduits do not advect with mantle flow as assumed in the GMHRF or Earth's actual mantle velocity field differs substantially from that assumed in constructing the GMHRF." Thus, there is good reason to suspect the reliability of the prediction that the Hawaiian hotspot was moving southeastward through the mantle from ≈80 to 50 Ma.

5.7 Influence of Geometry on Uncertainty in Inter-Hotspot Motion

The uncertainties on inter-hotspot distance tend to be much larger for 80–48 Ma than for 48 Ma to present (Figures 3D-E). Why is this so? When a given age uncertainty is mapped to location uncertainty, it contributes to the along-track component of uncertainty but not to the across-track component (Andrews et al., 2006; Wessel & Kroenke, 2008, 2009; Koivisto et al., 2014). Thus the dominant error in the location of an ancient hotspot is in the along-track component. During Hawaiian time, the main source of uncertainty for inter-hotspot distance is the small across-track uncertainty; during Emperor time it is the much larger along-track uncertainty (Figure S3). Furthermore, the age date dispersions are evidently larger for 80–48 Ma than for 48 Ma–present, there are some huge spatial gaps in age dates for Emperor-age volcanoes (Figure 2), as mentioned above, and there are merely eight age dates along the Emperor chain and merely eight age dates along the Emperor-age subtrack of the Louisville chain. These factors further contribute to larger uncertainties in inter-hotspot distance for 80–48 Ma than for 48 Ma to present.

5.8 Comparison with Rates of Hotspot Motion Between Ocean Basins

As discussed above, rates of motion between hotspots are low for the past 48 Ma whether estimated in a single ocean basin or between ocean basins (Wang et al., 2019a; Koivisto et al., 2014). For 68–48 Ma, however, the situation appears less simple. Using the plate motion circuit through Antarctica, Koivisto et al. (2014) found nominal rates of ≈50 mm/a ± ≈20 mm/a of motion between Indo-Atlantic hotspots and Pacific hotspots. These inter-ocean-basin rates are double the highest Pacific intra-ocean nominal rates of motion found herein over the same time interval and an order of magnitude larger than inter-hotspot motion rates in the Atlantic and Indian ocean basins and adjacent continents since Mesozoic time (Morgan, 1981; O'Neill et al., 2005). This comparison suggests either that Pacific hotspots, as a group, moved much faster relative to Indo-Atlantic hotspots than relative to other Pacific hotspots or that there are large systematic errors in the global plate circuit through Antarctica for reconstruction ages older than ≈48 Ma. While some workers favor high rates between ocean basins before ≈48 Ma (Norton, 1995; Raymond et al., 2000; Tarduno et al., 2003), paleomagnetic data indicate a flaw in the global plate motion circuit (Suárez & Molnar, 1980; Gordon & Cox, 1980; Acton & Gordon, 1994; Sager, 2007). When paleomagnetic poles from the continents are rotated into the Pacific plate reference frame through the plate circuit through Antarctica, the poles indicate less northward motion of the Pacific plate than do the indigenous Pacific plate paleomagnetic and other spin axis data (Suárez & Molnar, 1980; Gordon & Cox, 1980; Acton & Gordon, 1994).

Further support for a flaw in the early Cenozoic plate circuit through Antarctica comes from the work of Wessel and Conrad (2019), who compared hotspot tracks predicted in the Pacific basin from the motion of Africa over the hotspots combined with the global plate motion circuit through Antarctica. From the moving hotspot model of O'Neill et al. (2005), they found a nearly sinusoidal predicted hotspot drift with its most distal latitude at 60 Ma and then returning south for older ages. From a fixed hotspot model of Maher et al. (2015), they found a similar predicted pattern. Wessel and Conrad (2019) suggest that that the similar implied Pacific hotspot motion found from the two sets of Africa hotspot motion, which is inconsistent with observed paleolatitudes and with geodynamic models, may be an artifact of flaws in the plate motion circuit through Antarctica. A flaw in the early Cenozoic global plate motion circuit through Antarctica remains the best explanation of all the observations (Suárez & Molnar, 1980; Gordon & Cox, 1980; Acton & Gordon, 1994; Sager, 2007).

5.9 Nominal Plume Drift Relative to Absolute Reference Frames

Figures 5 and S5 show the nominal hotspot motion inferred from our preferred age models (i.e., those with coeval bends) for four estimates of Pacific plate motion, three of which are fixed Pacific hotspot reference frames and the fourth a global moving hotspot reference frame (GMHRF). A black-centered curve also shows Doubrovine et al. (2012)'s explicitly predicted motion of the Hawaii and Louisville hotspots relative to the GMHRF (Figure 5). (No predictions are shown for Rurutu because Doubrovine et al. (2012) make no predictions for it.) Despite having moving hotspots and many adjustable parameters, the GMHRF fits the age models no better than the much simpler fixed hotspot models, in particular GGW20. The GMHRF rotations fit Louisville about the same as GGW20 for the past 55 Ma, but worse before 55 Ma, and fit Hawaii worse than GGW20 for the past 65 Ma, but better from 80 to 65 Ma (Figures 5 and S5).

While it is tempting to attach physical significance to the nominal motions in Figure 5, none differ significantly from zero. Estimates of ≈50–70 mm/a of plume motion in catastrophic events such as migration of the Pacific large low shear velocity province (Tarduno et al., 2009; Hassan et al., 2016) are not supported by our results, but we cannot categorically exclude models that predict rates at the low end of that range.

5.10 Sequence and Timing of Important Eocene Tectonic Events

Combining our new estimate for the age of the Hawaiian-Emperor and Louisville bends, 47.4±1.0 Ma, with the latest age estimates of important Pacific and global tectonic events, our best estimate of the time sequence of the events (Figure 6 and Table S7) is as follows:

First, the following events preceded or largely preceded the age of the bends. Pacific-Kula motion changes direction at 57.1 Ma (C25y) (Lonsdale, 1988b). A major episode of Eocene true polar wander began no earlier than 54.0 Ma (C24o) and finished no later than 47.3 Ma (C21o) (Woodworth & Gordon, 2020). Nearly all spreading in the Tasman Sea ceased near 54.0 Ma (C24o) (Gaina et al., 1998). The Early Eocene Climate Optimum, which witnessed the highest sustained temperatures of the Cenozoic, occurred between 54.1 and 49.1 Ma (Westerhold et al., 2018). The Farallon-Vancouver breakup began 52.6 Ma (Figure 7) (C24.1y) (Atwater & Winterer, 1989; Lonsdale, 2005). Initiation of subduction along the Izu-Bonin-Marianas arc is dated as 52 to 48 Ma (Arculus et al., 2015). The onset of a decrease in spreading of the India plate relative to the Africa and Antarctica plates is dated at 49.3 Ma (C22o) (Figure 7) (Cande et al., 2010; Cande & Patriat, 2015). The initial collision of India with Eurasia (in the west of India) is dated at 51.7 to 48.7 Ma (Rowley, 1996; Bouilhol et al., 2013). The change in direction of spreading of the Pacific plate relative to the Vancouver and Farallon plates began at 51.8 Ma (and was completed at 45.7 Ma) (Figure 7) (Menard & Atwater, 1968; Barckhausen et al., 2013). Evidence documenting early New Caledonia trough formation and subsidence between 55 to 45 Ma combined with radiometric dates from the Tonga forearc showing arc activity starting between 52 and 48 Ma suggest the formation of a collisional margin between the Pacific and Australian plates (Meffre et al., 2012; Sutherland et al., 2020).

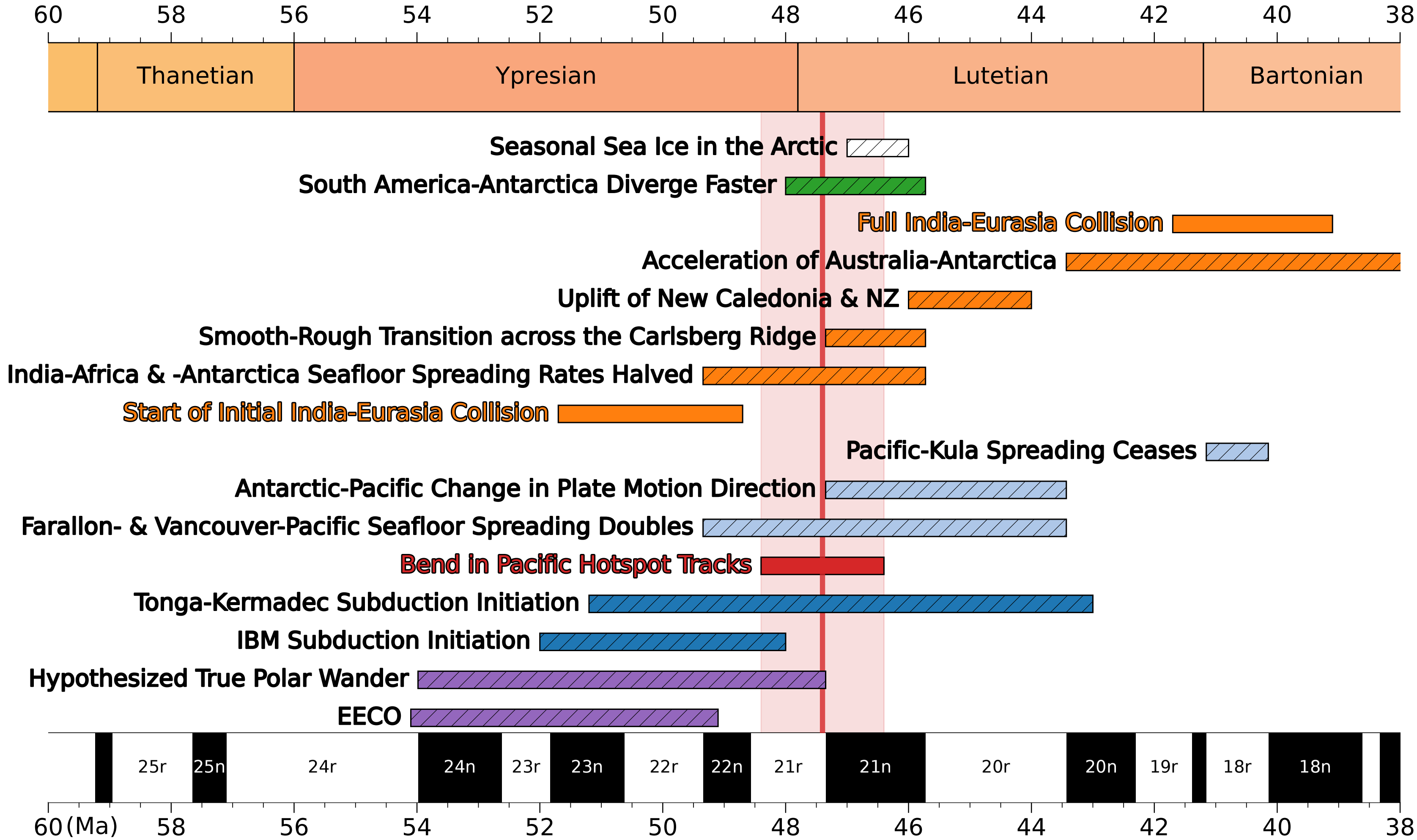

Figure 6. Timeline of selected Eocene tectonic and climatic events compared with our estimate of the age of the bends in Pacific plate hotspot tracks. Global events, purple; Pacific plate subduction initiation, dark blue; bend in Pacific plate hotspot tracks, red; change in Pacific plate relative motion, light blue; events mainly in the Indian Ocean, orange; events in Scotia Sea region, green; events in the Arctic, white. Diagonal hatching shows an age range of events. Unhatched events show a mean and uncertainty for the event rather than an age range. Source for geomagnetic reversal timescale and stage names: Gradstein et al. (2012).

Uplift of New Caledonia and New Zealand doesn't occur until 46 to 44 Ma, however, and plate motion changes between Australia and Antarctica do not occur until ≈43 Ma, during anomaly C20. Thus we bound Tonga-Kermadec (TK) subduction between 52 and 43 Ma based on the oldest dredged radiometric forarc ages and approximately the youngest uplift and relative plate motion change estimates. Some researchers have proposed a later initiation of TK subduction, between 45 and 30 Ma (van de Lagemaat et al., 2018), however. Opening of the Tasmanian gateway is dated 50 to 46 Ma (Bijl et al., 2013).

Second, the following events were coeval or nearly coeval with the 47.4±1.0 Ma bends: (1) The initiation of the doubling in spreading rate of the Pacific plate relative to the Farallon and Vancouver plates occurs at 47.3 Ma (C21o), simultaneous within measurement precision with the bend (Figure 7) (Barckhausen et al., 2013; D. S. Wilson, 2016), (2) Rifting of South America from the Antarctic Peninsula and initiation of Drake Passage opening occurred just before 47.3 Ma (C21o) (Livermore et al., 2005, 2007; Eagles, 2016), (3) The change in direction of motion between the Pacific and Antarctic plates occurred between 47.3 and 43.4 Ma (C21o and C20o) (Croon et al., 2008; Wright et al., 2016). (4) The rough-smooth boundary in bathymetry flanking the Carlsberg Ridge records the decrease through a threshold in full spreading rate near ≈60 mm/a (Small & Sandwell, 1992). The boundary is located between the C21o and C21y isochrons (Figure S7) and thus is dated as between 47.3 and 45.7 Ma. (5) The First appearance of ice rafted debris in the arctic ocean basin near 46 Ma (Stein, 2019).

Third, the following events all follow or mostly follow the age of the bends. The cessation of slowing of the India plate relative to the African and Antarctic plates is dated at 45.7 Ma (C21y) (Figure 7) (Cande et al., 2010; Cande & Patriat, 2015). The final collision of India with Eurasia (in the east of India) is dated between 41.7 and 39.1 Ma (Rowley, 1996; Bouilhol et al., 2013). Uplift of New Caledonia and New Zealand recording early convergence between the Pacific and Australian plates occurred 46-44 Ma (Dallanave et al., 2020). The rate of Australia-Antarctica spreading quadrupled between 43.4 and 33.7 Ma (≈C20o and C13o) (Figure 7) (Whittaker et al., 2007).

The most important inference about relative timing is that the initiation of subduction along the Izu-Bonin-Mariana arcs and the proto-Kermadec-Tonga arcs likely preceded the creation of the bends in the Hawaiian-Emperor and Louisville chains. These key results support the hypothesis that the formation of trenches subducting Pacific plate

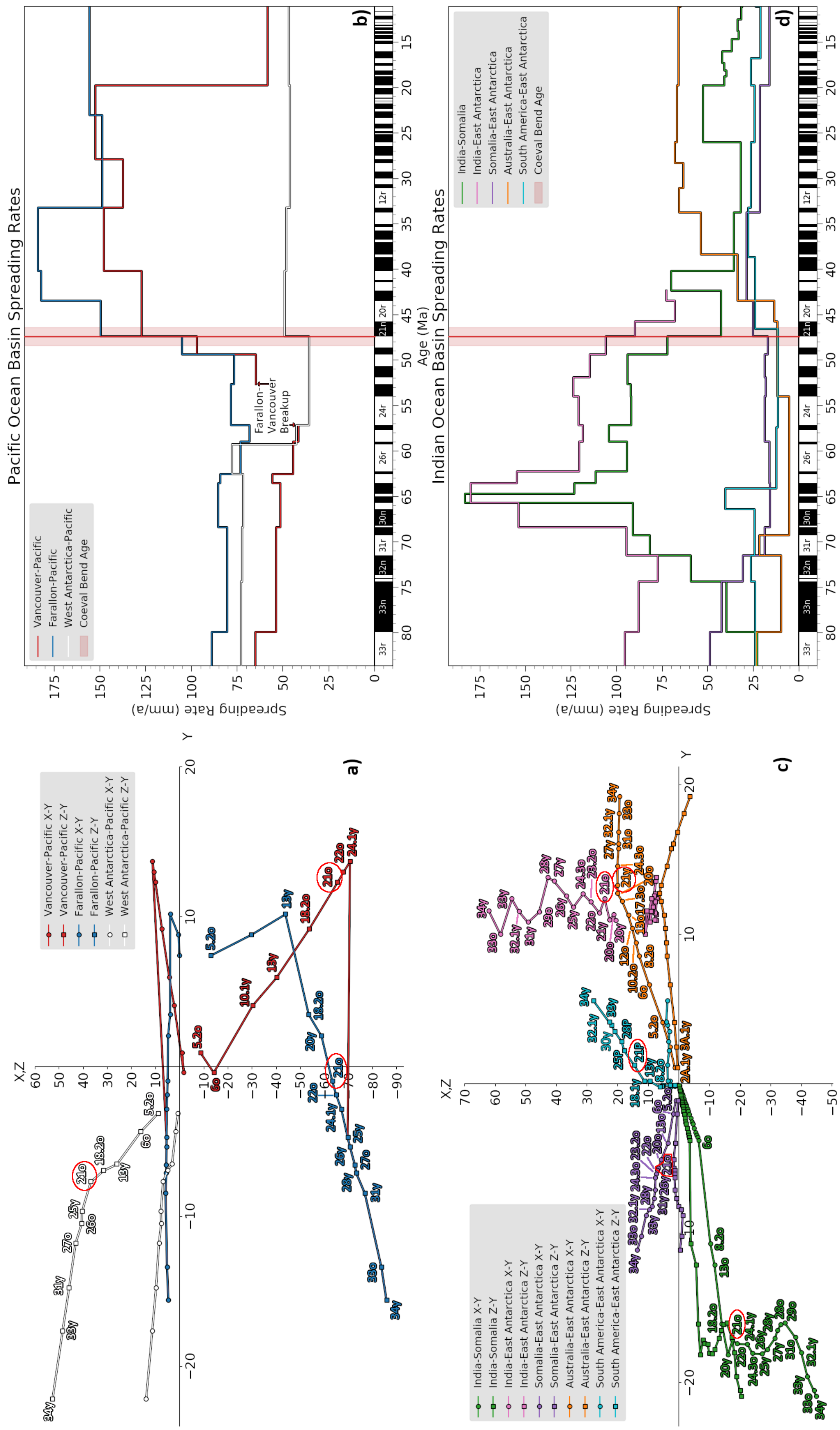
Pacific Ocean Basin Spreading Rates
Indian Ocean Basin Spreading Rates
Vancouver-Pacific X-Y
Vancouver-Pacific Z-Y
Farallon-Pacific X-Y
Farallon-Pacific Z-Y
West Antarctica-Pacific X-Y
West Antarctica-Pacific Z-Y
Vancouver-Pacific
Farallon-Pacific
West Antarctica-Pacific
Coeval Bend Age
Farallon-Vancouver Breakup
India-Somalia X-Y
India-Somalia Z-Y
India-East Antarctica X-Y
India-East Antarctica Z-Y
Somalia-East Antarctica X-Y
Somalia-East Antarctica Z-Y
Australia-East Antarctica X-Y
Australia-East Antarctica Z-Y
South America-East Antarctica X-Y
South America-East Antarctica Z-Y
India-Somalia
India-East Antarctica
Somalia-East Antarctica
Australia-East Antarctica
South America-East Antarctica
Coeval Bend Age
Spreading Rate (mm/a)
Age (Ma)
X,Z
Y
a)
b)
c)
d)

Figure 7. Vector endpoint diagrams of plate reconstruction rotations and spreading rate diagrams illustrating changes in relative plate motion near the coeval bend age of Pacific hotspot tracks. On the vector endpoint diagrams X, Y, and Z are the standard tectonic axes in the relevant reference frame (i.e. 0°N, 0°E; 0°N, 90°E; 90°N, 0°E respectively). 8a shows the Pacific and circum-Pacific relative plate motions in the Pacific reference frame between 34y and 5.2o from Wright et al. (2016); independent of timescale it shows a change in direction of spreading between West Antarctica-Pacific at 21o the reversal coincident with the coeval bend age. 8b shows implied spreading rate using timescale (Gradstein et al., 2012) rates are calculated starting at 42.09°N, 177.77°E, 3.18°N, 153.67°W, and 69.82°S, 101.49°W for Farallon, Vancouver, and West Antarctica relative to the Pacific plate respectively. These points correspond to magnetic picks for the oldest reversal in the reconstruction model used and are then moved by half a stage rotation each calculation. 8c shows the rotation vectors in the East Antarctic reference frame, except for India-Somalia which is in the Somalian reference frame, and 8d shows the spreading rates for other plate pairs outside the Pacific Ocean Basin (J. Royer & Patriat, 2002; Cande & Stock, 2004; Whittaker et al., 2007; Eagles & Hoang, 2014; Cande & Patriat, 2015; Eagles, 2016; DeMets et al., 2020). Rates are calculated similar to those in the Pacific Ocean Basin starting at reversals located at 14.37°S, 51.27°E, 52.42°S, 48.00°E, 60.98°S, 12.17°E, 63.00°S, 120.87°E, 65.27°S, 19.96°W for the plate pairs India-Somalia, India-East Antarctica, Somalia-East Antarctica, Australia-East Antarctica, South America- East Antarctica respectively.

lithosphere in the western and southwestern Pacific basin was the cause of the change in torque on the Pacific plate that induced the westward change in Pacific plate velocity that was in turn the cause of the bend in the Hawaiian-Emperor chain (Gordon et al., 1978). The second most important inference is that the initiation of the speed up of Pacific-Farallon spreading rate coincides, within the limits of precision, with the age of the bend (Figure 7), as is expected if the bend is due to a westward change in the direction of Pacific plate motion relative to the deep mantle. Other important findings are that Eocene true polar wander almost surely precedes the bend (Woodworth & Gordon, 2020), that the onset of the slowdown of India relative to Africa and Antarctica (presumably related to the initial collision of India and Eurasia) precedes the bend whereas the cessation of the slowdown is younger than the bend. Any causal connection between the slowdown of India and the Eocene bend in Pacific plate hotspot chains is unclear.

6 Conclusions

1. Ten adjustable parameters, six for the spatial fit and four for the age fit, adequately fit the space-time progression of an individual Pacific plate hotspot track over the past ≈80 Ma.
2. The location of the Hawaiian-Emperor bend (HEB) is well constrained, that of the Louisville bend (LB) is loosely constrained, and that of the Rurutu bend is unconstrained by available volcano locations and age dates.
3. Our results do not preclude motion between these three hotspots over the past ≈80 Ma, but estimated motions differ insignificantly from zero. Thus, interpretations of these nominal motions are likely premature. The limits we place on motion between these hotspots are small enough to exclude some hypotheses that attribute the origin of the HEB to a change in hotspot or plume motion if the Louisville hotspot is assumed to have been fixed.
4. The motions of hotspots predicted by the Global Moving Hotspot Reference Frame fit observed Pacific hotspot tracks no better than simply assuming fixed hotspots.
5. Prior work that inferred a significant difference in age between the Hawaiian-Emperor Bend and the Louisville Bend (LB) neglected the uncertainty in the location of the LB. When that uncertainty is incorporated, there is no significant difference in age between the two bends.

6. The best estimate of the age of an assumed-coeval bend in Pacific hotspot chains, 47.4±1.0, is coeval with the onset of doubling of the spreading rate of the Pacific plate relative to the Farallon and Vancouver plates.
7. The bend is preceded by the initiation of the slowdown of India motion relative to Africa and Antarctica, but followed by the cessation of that same slowdown.
8. The bend age is a few millions years younger than the initiation of subduction along the western and possibly the southwestern Pacific boundaries of the Pacific plate, consistent with subduction initiation changing the torque on the Pacific plate such that it started moving in a more westward direction thus creating the bends in the Hawaiian-Emperor and other Pacific plate hotspot chains (Gordon et al., 1978).

Acknowledgments

We thank L. Boschman and an anonymous reviewer for comments that helped us to improve this paper. We thank K. Konrad for his quick and cordial replies to our questions regarding his data and methods. We thank Jerry Dickens for many helpful discussions on the timing of Eocene paleo-oceanographic and paleoclimate events. This work was partly supported by U.S. National Science Foundation grant OCE-1559316. All data used here are contained entirely in the cited references and detailed in the supplement. The code and data that produced these results can be found online at https://github.com/Rice-Tectonics-Group/Quantification-of-PacificPlate-Hotspot-Tracks.

References

Acton, G. D., & Gordon, R. G. (1991). A 65 ma palaeomagnetic pole for the pacific plate from the skewness of magnetic anomalies 27r-31. *Geophysical Journal International*, *106*(2), 407–420.

Acton, G. D., & Gordon, R. G. (1994). Paleomagnetic tests of pacific plate reconstructions and implications for motion between hotspots. *Science*, *263*(5151), 1246–1254.

Andrews, D. L., Gordon, R. G., & Horner-Johnson, B. C. (2006). Uncertainties in plate reconstructions relative to the hotspots; pacific-hotspot rotations and uncertainties for the past 68 million years. *Geophysical Journal International*, *166*(2), 939–951.

Arculus, R. J., Ishizuka, O., Bogus, K. A., Gurnis, M., Hickey-Vargas, R., Aljahdali, M. H., ... others (2015). A record of spontaneous subduction initiation in the izu–bonin–mariana arc. *Nature Geoscience*, *8*(9), 728–733.

Atwater, T., & Winterer, E. (1989). Plate tectonic history of the northeast pacific and western north america. *The Eastern Pacific Ocean and Hawaii*, 21–72.

Austermann, J., Ben-Avraham, Z., Bird, P., Heidbach, O., Schubert, G., & Stock, J. M. (2011). Quantifying the forces needed for the rapid change of pacific plate motion at 6 ma. *Earth and Planetary Science Letters*, *307*(3-4), 289–297.

Barckhausen, U., Bagge, M., & Wilson, D. S. (2013). Seafloor spreading anomalies and crustal ages of the clarion-clipperton zone. *Marine Geophysical Research*, *34*(2), 79–88.

Bevington, P. (1969). *Data reduction and error analysis for the physical sciences.* McGraw-Hill Book Company, New York.

Bijl, P. K., Bendle, J. A., Bohaty, S. M., Pross, J., Schouten, S., Tauxe, L., ... others (2013). Eocene cooling linked to early flow across the tasmanian gateway. *Proceedings of the National Academy of Sciences*, *110*(24), 9645–9650.

Boas, M. L. (2006). *Mathematical methods in the physical sciences.* John Wiley & Sons.

Bono, R. K., Tarduno, J. A., & Bunge, H.-P. (2019). Hotspot motion caused the hawaiian-emperor bend and llsvps are not fixed. *Nature communications*, *10*(1), 3370.

Bouilhol, P., Jagoutz, O., Hanchar, J. M., & Dudas, F. O. (2013). Dating the india–eurasia collision through arc magmatic records. *Earth and Planetary Science Letters*, *366*, 163–175.

Cande, S. C., & Patriat, P. (2015). The anticorrelated velocities of africa and india in the late cretaceous and early cenozoic. *Geophysical Journal International*, *200*(1), 227–243.

Cande, S. C., Patriat, P., & Dyment, J. (2010). Motion between the indian, antarctic and african plates in the early cenozoic. *Geophysical Journal International*, *183*(1), 127–149.

Cande, S. C., & Stock, J. M. (2004). Pacific—antarctic—australia motion and the formation of the macquarie plate. *Geophysical Journal International*, *157*(1), 399–414.

Cox, A., & Engebretson, D. (1985). Change in motion of pacific plate at 5 myr bp. *Nature*, *313*(6002), 472–474.

Cox, A., & Gordon, R. G. (1984). Paleolatitudes determined from paleomagnetic data from vertical cores. *Reviews of Geophysics*, *22*(1), 47–72.

Croon, M. B., Cande, S. C., & Stock, J. M. (2008). Revised pacific-antarctic plate motions and geophysics of the menard fracture zone. *Geochemistry, Geophysics, Geosystems*, *9*(7).

Dallanave, E., Maurizot, P., Agnini, C., Sutherland, R., Hollis, C. J., Collot, J., ... Morgans, H. E. (2020). Eocene (46–44 ma) onset of australia-pacific plate motion in the southwest pacific inferred from stratigraphy in new caledonia and new zealand. *Geochemistry, Geophysics, Geosystems*, *21*(7), e2019GC008699.

Dalrymple, G. B., & Clague, D. (1976). Age of the hawaiian-emperor bend. *Earth and Planetary Science Letters*, *31*(3), 313–329.

Dalrymple, G. B., Silver, E. A., & Jackson, E. D. (1973). Origin of the hawaiian islands: Recent studies indicate that the hawaiian volcanic chain is a result of relative motion between the pacific plate and a melting spot in the earth's mantle. *American Scientist*, *61*(3), 294–308.

DeMets, C., & Merkouriev, S. (2016). High-resolution reconstructions of pacific–north america plate motion: 20 ma to present. *Geophysical Journal International*, *207*(2), 741–773.

DeMets, C., Merkouriev, S., & Jade, S. (2020). High-resolution reconstructions and gps estimates of india–eurasia and india–somalia plate motions: 20 ma to the present. *Geophysical Journal International*, *220*(2), 1149–1171.

Doubrovine, P. V., Steinberger, B., & Torsvik, T. H. (2012). Absolute plate motions in a reference frame defined by moving hot spots in the pacific, atlantic, and indian oceans. *Journal of Geophysical Research: Solid Earth*, *117*(B9).

Eagles, G. (2016). Plate kinematics of the rocas verdes basin and patagonian orocline. *Gondwana Research*, *37*, 98–109.

Eagles, G., & Hoang, H. H. (2014). Cretaceous to present kinematics of the indian, african and seychelles plates. *Geophysical Journal International*, *196*(1), 1–14.

Epp, D. (1978). Relationships between plate-plate and plate-mantle motion in pacific. In *Transactions-american geophysical union* (Vol. 59, pp. 1203–1203).

Finlayson, V., Konter, J., Konrad, K., Koppers, A., Jackson, M., & Rooney, T. (2018). Sr–pb–nd–hf isotopes and 40ar/39ar ages reveal a hawaii–emperor-style bend in the rurutu hotspot. *Earth and Planetary Science Letters*, *500*, 168–179.

Fritsch, F. N., & Carlson, R. E. (1980). Monotone piecewise cubic interpolation. *SIAM Journal on Numerical Analysis*, *17*(2), 238–246.

Gaina, C., Müller, D. R., Royer, J.-Y., Stock, J., Hardebeck, J., & Symonds, P. (1998). The tectonic history of the tasman sea: a puzzle with 13 pieces. *Journal of Geophysical Research: Solid Earth*, *103*(B6), 12413–12433.

Gordon, R. G., & Cape, C. D. (1981). Cenozoic latitudinal shift of the hawaiian hotspot and its implications for true polar wander. *Earth and Planetary Science Letters*, *55*(1), 37–47.

Gordon, R. G., & Cox, A. (1980). Paleomagnetic test of the early tertiary plate circuit between the pacific basin plates and the indian plate. *Journal of Geophysical Research: Solid Earth*, *85*(B11), 6534–6546.

Gordon, R. G., Cox, A., & Harter, C. E. (1978). Absolute motion of an individual plate estimated from its ridge and trench boundaries. *Nature*, *274*(5673), 752–755.

Gordon, R. G., Cox, A., & O'Hare, S. (1984). Paleomagnetic euler poles and the apparent polar wander and absolute motion of north america since the carboniferous. *Tectonics*, *3*(5), 499–537.

Gradstein, F. M., Ogg, J. G., Schmitz, M. B., & Ogg, G. M. (2012). *The geologic* *time scale 2012*. elsevier.

Gripp, A. E., & Gordon, R. G. (2002). Young tracks of hotspots and current plate velocities. *Geophysical Journal International*, *150*(2), 321–361.

Hassan, R., Müller, R. D., Gurnis, M., Williams, S. E., & Flament, N. (2016). A rapid burst in hotspot motion through the interaction of tectonics and deep mantle flow. *Nature*, *533*(7602), 239.

Hayes, D. E., & Ewing, M. (1971). The louisville ridge—a possible extention of the eltanin fracture zone. *Antarctic oceanology I*, *15*, 223–228.

Heaton, D., & Koppers, A. (2019). High-resolution 40ar/39ar geochronology of the louisville seamounts iodp expedition 330 drill sites: Implications for the duration of hot spot-related volcanism and age progressions. *Geochemistry, Geophysics, Geosystems*.

Irving, E. (1964). *Paleomagnetism and its application to geological and geophysical problems*. New York: Wiley.

Jackson, E., Koizumi, I., Dalrymple, G., Clague, D., Kirkpatrick, R., & Greene, H. (1980). Introduction and summary of results from dsdp leg 55, the hawaiian-emperor hot-spot experiment. *Initial reports of the deep sea drilling project*, *55*, 5–31.

Koivisto, E. A., Andrews, D. L., & Gordon, R. G. (2014). Tests of fixity of the indo-atlantic hot spots relative to pacific hot spots. *Journal of Geophysical Research: Solid Earth*, *119*(1), 661–675.

Kono, M. (1980). Paleomagnetism of dsdp leg 55 basalts and implications for the tectonics of the pacific plate. *Initial Reports of the Deep Sea Drilling Project*, *55*, 737–752.

Konrad, K., Koppers, A. A., Steinberger, B., Finlayson, V. A., Konter, J. G., & Jackson, M. G. (2018). On the relative motions of long-lived pacific mantle plumes. *Nature communications*, *9*(1), 854.

Koppers, A. A., Gowen, M. D., Colwell, L. E., Gee, J. S., Lonsdale, P. F., Mahoney, J. J., & Duncan, R. A. (2011). New 40ar/39ar age progression for the louisville hot spot trail and implications for inter–hot spot motion. *Geochemistry, Geophysics, Geosystems*, *12*(12).

Koppers, A. A., & Staudigel, H. (2005). Asynchronous bends in pacific seamount trails: a case for extensional volcanism? *Science*, *307*(5711), 904–907.

Koppers, A. A., Staudigel, H., & Minnett, R. (2010). Seamount catalog: seamount morphology, maps, and data files. *Oceanography*.

Livermore, R., Hillenbrand, C.-D., Meredith, M., & Eagles, G. (2007). Drake passage and cenozoic climate: an open and shut case? *Geochemistry, Geophysics, Geosystems*, *8*(1).

Livermore, R., Nankivell, A., Eagles, G., & Morris, P. (2005). Paleogene opening of drake passage. *Earth and Planetary Science Letters*, *236*(1-2), 459–470.

Lonsdale, P. (1988a). Geography and history of the louisville hotspot chain in the southwest pacific. *Journal of Geophysical Research: Solid Earth*, *93*(B4), 3078–3104.

Lonsdale, P. (1988b). Paleogene history of the kula plate: Offshore evidence and onshore implications. *Geological Society of America Bulletin*, *100*(5), 733–754.

Lonsdale, P. (2005). Creation of the cocos and nazca plates by fission of the farallon plate. *Tectonophysics*, *404*(3-4), 237–264.

Maher, S., Wessel, P., Müller, R., Williams, S., & Harada, Y. (2015). Absolute plate motion of africa around hawaii-emperor bend time. *Geophysical Journal International*, *201*(3), 1743–1764.

May, S. R., & Butler, R. F. (1986). North american jurassic apparent polar wander: Implications for plate motion, paleogeography and cordilleran tectonics. *Journal of Geophysical Research: Solid Earth*, *91*(B11), 11519–11544.

McKenzie, D. (2018). A geologist reflects on a long career. *Annual Review of Earth and Planetary Sciences*, *46*, 1–20.

Meffre, S., Falloon, T. J., Crawford, T. J., Hoernle, K., Hauff, F., Duncan, R. A., ... Wright, D. J. (2012). Basalts erupted along the tongan fore arc during subduction initiation: Evidence from geochronology of dredged rocks from the tonga fore arc and trench. *Geochemistry, Geophysics, Geosystems*, *13*(12).

Menard, H., & Atwater, T. (1968). Changes in direction of sea floor spreading. *Nature*, *219*(5153), 463–467.

Molnar, P., & Stock, J. (1987). Relative motions of hotspots in the pacific, atlantic and indian oceans since late cretaceous time. *Nature*, *327*(6123), 587–591.

Moore, J. G., Decker, R., Wright, T., & Stauffer, P. (1987). Subsidence of the hawaiian ridge. *US Geol. Surv. Prof. Pap*, *1350*(1), 85–100.

Morgan, W. J. (1972). Deep mantle convection plumes and plate motions. *AAPG* *bulletin*, *56*(2), 203–213.

Morgan, W. J. (1981). 13. hotspot tracks and the opening of the atlantic and indian oceans. *The oceanic lithosphere*, *7*, 443.

Morgan, W. J., & Morgan, J. P. (2007). Plate velocities in the hotspot reference frame. *SPECIAL PAPERS-GEOLOGICAL SOCIETY OF AMERICA*, *430*, 65.

Nelder, J. A., & Mead, R. (1965). A simplex method for function minimization. *The computer journal*, *7*(4), 308–313.

Norton, I. O. (1995). Plate motions in the north pacific: the 43 ma nonevent. *Tectonics*, *14*(5), 1080–1094.

O'Connor, J. M., Steinberger, B., Regelous, M., Koppers, A. A., Wijbrans, J. R., Haase, K. M., ... Garbe-Schönberg, D. (2013). Constraints on past plate and mantle motion from new ages for the hawaiian-emperor seamount chain. *Geochemistry, Geophysics, Geosystems*, *14*(10), 4564–4584.

O'Neill, C., Müller, D., & Steinberger, B. (2005). On the uncertainties in hot spot reconstructions and the significance of moving hot spot reference frames. *Geochemistry, Geophysics, Geosystems*, *6*(4).

Petronotis, K. E., Gordon, R. G., & Acton, G. D. (1994). A 57 ma pacific plate palaeomagnetic pole determined from a skewness analysis of crossings of marine magnetic anomaly 25r. *Geophysical Journal International*, *118*(3), 529–554.

Pollitz, F. F. (1986). Pliocene change in pacific-plate motion. *Nature*, *320*(6064), 738–741.

Press, W. H., Flannery, B. P., Teukolsky, S. A., & Vetterling, W. T. (1986). Numerical recipes: The art of scientific computing((book)). *Cambridge and New York, Cambridge University Press, 1986, 839*.

Raymond, C. A., Stock, J. M., & Cande, S. C. (2000). Fast paleogene motion of the pacific hotspots from revised global plate circuit constraints. *The History and Dynamics of Global Plate Motions*, *121*, 359–375.

Rowley, D. B. (1996). Age of initiation of collision between india and asia: A review of stratigraphic data. *Earth and Planetary Science Letters*, *145*(1-4), 1–13.

Royer, J., & Patriat, P. (2002). L'inde part a la derive. *Himalaya-Tibet, Le choc des continents*, 25–31.

Royer, J.-Y., & Chang, T. (1991). Evidence for relative motions between the indian and australian plates during the last 20 my from plate tectonic reconstructions: Implications for the deformation of the indo-australian plate. *Journal of Geophysical Research: Solid Earth*, *96*(B7), 11779–11802.

Sager, W. W. (2007). Divergence between paleomagnetic and hotspot-model–predicted polar wander for the pacific plate with implications for hotspot fixity. *Plates, Plumes, and Planetary Processes*, *430*, 335.

Sandwell, D. T., Müller, R. D., Smith, W. H., Garcia, E., & Francis, R. (2014). New global marine gravity model from cryosat-2 and jason-1 reveals buried tectonic structure. *Science*, *346*(6205), 65–67.

Sharp, W. D., & Clague, D. A. (2006). 50-ma initiation of hawaiian-emperor bend records major change in pacific plate motion. *Science*, *313*(5791), 1281–1284.

Small, C., & Sandwell, D. T. (1992). An analysis of ridge axis gravity roughness and spreading rate. *Journal of Geophysical Research: Solid Earth*, *97*(B3), 3235–3245.

Stein, R. (2019). The late mesozoic-cenozoic arctic ocean climate and sea ice history: A challenge for past and future scientific ocean drilling. *Paleoceanography and Paleoclimatology*, *34*(12), 1851–1894.

Steinberger, B., & O'Connell, R. J. (1998). Advection of plumes in mantle flow: implications for hotspot motion, mantle viscosity and plume distribution. *Geophysical Journal International*, *132*(2), 412–434.

Suárez, G., & Molnar, P. (1980). Paleomagnetic data and pelagic sediment facies and the motion of the pacific plate relative to the spin axis since the late cretaceous. *Journal of Geophysical Research: Solid Earth*, *85*(B10), 5257–5280.

Sutherland, R., Dickens, G. R., Blum, P., Agnini, C., Alegret, L., Asatryan, G., … others (2020). Continental-scale geographic change across zealandia during paleogene subduction initiation. *Geology*, *48*(5), 419–424.

Tarduno, Bunge, H.-P., Sleep, N., & Hansen, U. (2009). The bent hawaiian-emperor hotspot track: Inheriting the mantle wind. *Science*, *324*(5923), 50–53.

Tarduno, Duncan, R. A., Scholl, D. W., Cottrell, R. D., Steinberger, B., Thordarson, T., … others (2003). The emperor seamounts: Southward motion of the hawaiian hotspot plume in earth's mantle. *Science*, *301*(5636), 1064–1069.

Torsvik, T. H., Doubrovine, P. V., Steinberger, B., Gaina, C., Spakman, W., &

Domeier, M. (2017). Pacific plate motion change caused the hawaiian-emperor bend. *Nature communications*, *8*, 15660.

van de Lagemaat, S. H., Van Hinsbergen, D. J., Boschman, L. M., Kamp, P. J., & Spakman, W. (2018). Southwest pacific absolute plate kinematic reconstruction reveals major cenozoic tonga-kermadec slab dragging. *Tectonics*, *37*(8), 2647–2674.

Wang, C., Gordon, R. G., & Zhang, T. (2017). Bounds on geologically current rates of motion of groups of hot spots. *Geophysical Research Letters*, *44*(12), 6048–6056.

Wang, C., Gordon, R. G., Zhang, T., & Zheng, L. (2019a). Uncertainties in trends of young hotspot tracks. *Geophysical Research Letters*.

Wang, C., Gordon, R. G., Zhang, T., & Zheng, L. (2019b). Observational test of the global moving hotspot reference frame. *Geophysical Research Letters*.

Watts, A., Weissel, J., Duncan, R. A., & Larson, R. (1988). Origin of the louisville ridge and its relationship to the eltanin fracture zone system. *Journal of Geophysical Research: Solid Earth*, *93*(B4), 3051–3077.

Wessel, P., & Conrad, C. P. (2019). Assessing models for pacific absolute plate and plume motions. *Geochemistry, Geophysics, Geosystems*.

Wessel, P., & Kroenke, L. W. (2008). Pacific absolute plate motion since 145 ma: An assessment of the fixed hot spot hypothesis. *Journal of Geophysical Research: Solid Earth*, *113*(B6).

Wessel, P., & Kroenke, L. W. (2009). Observations of geometry and ages constrain relative motion of hawaii and louisville plumes. *Earth and Planetary Science Letters*, *284*(3-4), 467–472.

Westerhold, T., Röhl, U., Donner, B., & Zachos, J. C. (2018). Global extent of early eocene hyperthermal events: A new pacific benthic foraminiferal isotope record from shatsky rise (odp site 1209). *Paleoceanography and Paleoclimatology*, *33*(6), 626–642.

Whittaker, J., Müller, R., Leitchenkov, G., Stagg, H., Sdrolias, M., Gaina, C., & Goncharov, A. (2007). Major australian-antarctic plate reorganization at hawaiian-emperor bend time. *Science*, *318*(5847), 83–86.

Wilson, D. S. (2016). Revision of paleogene plate motions in the pacific and implications for the hawaiian-emperor bend: Comment. *Geology*, *44*(4), e384–e384.

Wilson, J. T. (1963). A possible origin of the hawaiian islands. *Canadian Journal of Physics*, *41*(6), 863–870.

Woodworth, D., & Gordon, R. G. (2020). Timing of eocene true polar wander inferred from pacific plate marine magnetic anomalies. In *Agu fall meeting 2020.*

Wright, N. M., Seton, M., Williams, S. E., & Mueller, R. D. (2016). The late cretaceous to recent tectonic history of the pacific ocean basin. *Earth-Science Reviews*, *154*, 138–173.

Supporting Information for "Quantification of Pacific Plate Hotspot Tracks Since 80 Ma and the Relative Timing of Eocene Plate Tectonic Events"

Kevin M. Gaastra[1], Richard G. Gordon[1], and Daniel T. Woodworth[1]

[1]Department of Earth, Environmental, and Planetary Sciences, Rice University, Houston, Texas USA

Contents of this file

Additional Supporting Information (Files uploaded separately)

1. Table S5 in file seamount_ages_input.xlsx
2. Table S6 in file PA_nhotspot_inversion.csv
3. Table S7 in file Events_Near_HEB.xlsx

Introduction

This supporting information file further documents the age models in which the bends in Pacific hotspot tracks are constrained to be coeval and also documents the age models in which the bends are not constrained to be coeval. Figure S1 shows the geographic and age models constructed for all three hotspot chains in the case where the bends are not constrained to be coeval. Figure S2 shows how the individual small circles defining each Pacific hotspot subtrack differ from the relevant subtrack stage rotation in the Pacific plate reference frame. The difference in the orientation of the error ellipse relative to the great circle connecting the Hawaiian, Rurutu, and Louisville hotspot tracks is shown in Figure S3 for ages 25 Ma and 58 Ma. The results of the numerical search for the age of the bends in the Hawaiian, Rurutu, and Louisville hotspot tracks is displayed in Figure S4, which details the contribution from both subtracks of each of the three chains respectively to the total misfit. Figure S5 shows the plume drift from present day location as a function of time estimated from these age models after subtracting either the GGW20, KAG14, WK08-A, or GMHRF rotations. Figure S6 shows the evolution of the location of the poles of rotation between the Pacific plate and Pacific hotspots in the Pacific plate reference frame from 0 Ma to 80 Ma for the case in which the bends are constrained to be coeval. Evidence used in our estimation of the approximate age (between C21o and C21y) of the smooth to rough seafloor transition across the Carlsberg ridge based on the vertical gravity gradient of (Sandwell et al., 2014) and the isochrons estimated by (Cande et al., 2010) and (Eagles & Hoang, 2014) is shown in Figure S7. Table S1 lists the small circles and bend locations determined in the geographic inversions detailed in the manuscript.

Table S2 contains the summed squared misfits, degrees of freedom, and statistics used to test for higher order polynomial models in the age progressions used in the manuscript. Table S3 and S4 detail the inverted parameters as well as their variances and covariances determined for the age models of the Hawaiian, Rurutu, and Louisville hotspots. The input data used to construct these geographic and age progressions are detailed in Table S5 (in file seamount_ages_input.xlsx). Table S6 (in file PA_nhotspot_inversion.csv) presents our Pacific plate-hotspot finite rotations determined from the geographic and age models in Figure 1 and 2 of the manuscript using the N-hotspot method of Andrews, Gordon, and Horner-Johnson (2006). The covariance matrix is parameterized analogously to the parameterizations of (Chang, 1988) and explained in the caption below. Table S7 (in file Events_Near_HEB.xlsx) collects the sequence of major Eocene tectonic events around the age of the bends in Pacific hotspots and their sources.

References

Andrews, D. L., Gordon, R. G., & Horner-Johnson, B. C. (2006). Uncertainties in plate reconstructions relative to the hotspots; pacific-hotspot rotations and uncertainties for the past 68 million years. *Geophysical Journal International*, *166*(2), 939–951.

Cande, S. C., Patriat, P., & Dyment, J. (2010). Motion between the indian, antarctic and african plates in the early cenozoic. *Geophysical Journal International*, *183*(1), 127–149.

Chang, T. (1988). Estimating the relative rotation of two tectonic plates from boundary crossings. *Journal of the American Statistical Association*, *83*(404), 1178–1183.

Doubrovine, P. V., Steinberger, B., & Torsvik, T. H. (2012). Absolute plate motions in a reference frame defined by moving hot spots in the pacific, atlantic, and indian oceans. *Journal of Geophysical Research: Solid Earth*, *117*(B9).

Eagles, G., & Hoang, H. H. (2014). Cretaceous to present kinematics of the indian, african and seychelles plates. *Geophysical Journal International*, *196*(1), 1–14.

Finlayson, V., Konter, J., Konrad, K., Koppers, A., Jackson, M., & Rooney, T. (2018). Sr–pb–nd–hf isotopes and 40ar/39ar ages reveal a hawaii–emperor-style bend in the rurutu hotspot. *Earth and Planetary Science Letters*, *500*, 168–179.

Heaton, D., & Koppers, A. (2019). High-resolution 40ar/39ar geochronology of the louisville seamounts iodp expedition 330 drill sites: Implications for the duration of hot spot-related volcanism and age progressions. *Geochemistry, Geophysics, Geosystems*.

Koivisto, E. A., Andrews, D. L., & Gordon, R. G. (2014). Tests of fixity of the indo-atlantic hot spots relative to pacific hot spots. *Journal of Geophysical Research: Solid Earth*, *119*(1), 661–675.

Sandwell, D. T., Müller, R. D., Smith, W. H., Garcia, E., & Francis, R. (2014). New global marine gravity model from cryosat-2 and jason-1 reveals buried tectonic structure. *Science*, *346*(6205), 65–67.

Wessel, P., & Kroenke, L. W. (2008). Pacific absolute plate motion since 145 ma: An assessment of the fixed hot spot hypothesis. *Journal of Geophysical Research: Solid Earth*, *113*(B6).

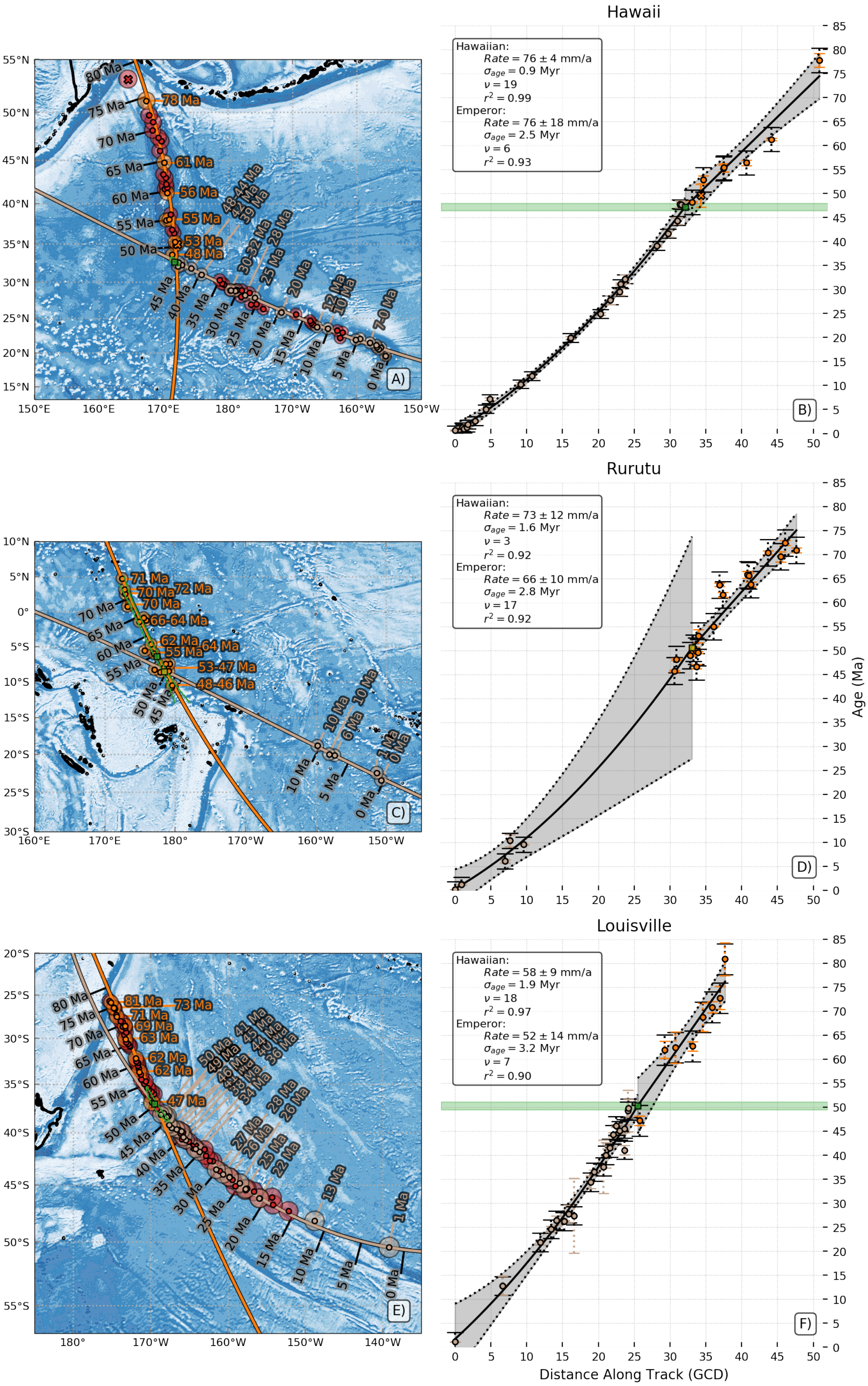
Hawaii
Hawaiian:
$Rate = 76 \pm 4$ mm/a
$\sigma_{age} = 0.9$ Myr
$\nu = 19$
$r^2 = 0.99$
Emperor:
$Rate = 76 \pm 18$ mm/a
$\sigma_{age} = 2.5$ Myr
$\nu = 6$
$r^2 = 0.93$
A)
B)
Rurutu
Hawaiian:
$Rate = 73 \pm 12$ mm/a
$\sigma_{age} = 1.6$ Myr
$\nu = 3$
$r^2 = 0.92$
Emperor:
$Rate = 66 \pm 10$ mm/a
$\sigma_{age} = 2.8$ Myr
$\nu = 17$
$r^2 = 0.92$
C)
D)
Louisville
Hawaiian:
$Rate = 58 \pm 9$ mm/a
$\sigma_{age} = 1.9$ Myr
$\nu = 18$
$r^2 = 0.97$
Emperor:
$Rate = 52 \pm 14$ mm/a
$\sigma_{age} = 3.2$ Myr
$\nu = 7$
$r^2 = 0.90$
E)
F)
Age (Ma)
Distance Along Track (GCD)

Figure S1. Hotspot geographic and age models for the Hawaiian-Emperor, Rurutu, and Louisville chains when the bends in these three chains are not constrained to be coeval. **A**, **C**, and **E** show the small circles that best fit the seamount locations of both the Hawaiian- (tan) and Emperor-age (orange) subtracks atop the gravity grid of Sandwell et al. (2014). The orange- or tan-filled circles are locations of dated seamounts assigned respectively to the Hawaiian and Emperor subtracks; red-filled circles are locations of undated seamounts. Orange numerals are nominal ages of dated seamounts; black numerals are the age of the hotspot-track model. **B**, **D**, and **F** show the hotspot age models plus uncertainties in age. Solid orange error bars are analytical 2-sigma uncertainties; dotted orange error bars are age dates for seamounts with more than one date (Table 2 of Heaton and Koppers (2019)); dashed black error bars are the age uncertainty determined from the dispersion of the age dates. Crosses show locations of seamounts with age dates excluded from analysis. Green-filled squares show maximum likelihood bend locations; green contours show their two sigma uncertainties. Yellow-filled square in **C** and **D** shows the Rurutu bend location of Finlayson et al. (2018). Rates given for the quadratic models of the Hawaiian subtrack represent the mean over Hawaiian time (0–47.4 Ma).

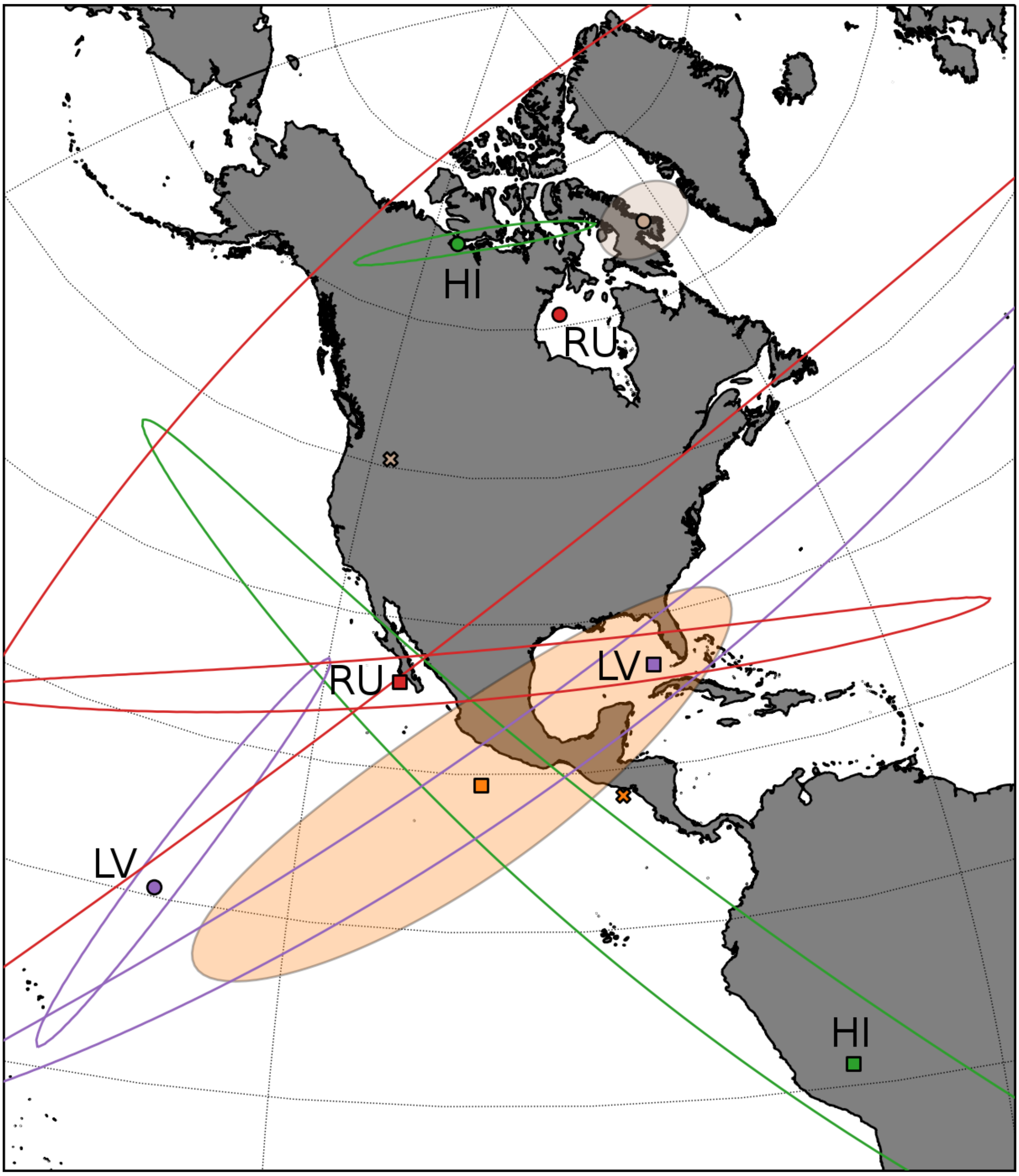

Figure S2. Poles to the best-fit small circles for each subtrack of the Hawaiian (HI: green), Louisville (LV: purple), and Rurutu (RU: red) hotspot tracks. Color-filled circles, Hawaiian subtrack; color-filled squares, Emperor subtrack. 2-sigma uncertainties are shown by ellipsoidal curves. Hawaii-age subtrack rotation pole, tan with shaded uncertainty; Emperor-age stage pole (Pacific plate reference frame), orange-filled square with shaded uncertainty. Fisher means of the small circle poles, X's (tan, Hawaiian subtracks; orange, Emperor subtracks).

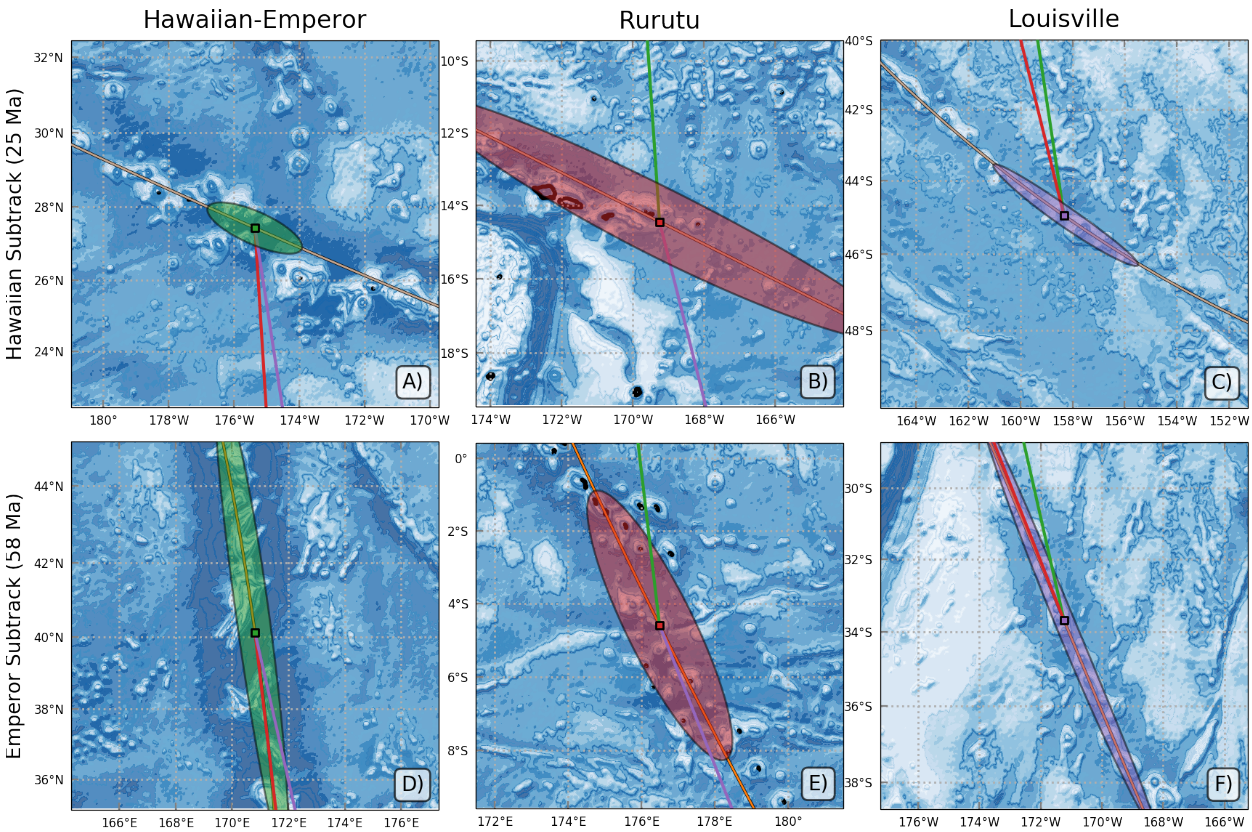

Figure S3. Uncertainty ellipses for locations corresponding to ages of 25 Ma and 58 Ma for each of the Hawaii, Rurutu, and Louisville hotspot tracks. A great circle connects a 25 Ma-old (**A**, **B**, **C**) or 58 Ma-old (**D**, **E**, **F**) point on a hotspot track to the coeval point on another track. E.g., the red great circle in **A** connects the 25-Ma point along the Hawaii track to the coeval point along the Rurutu track in **B**, in which the same great circle is colored green.

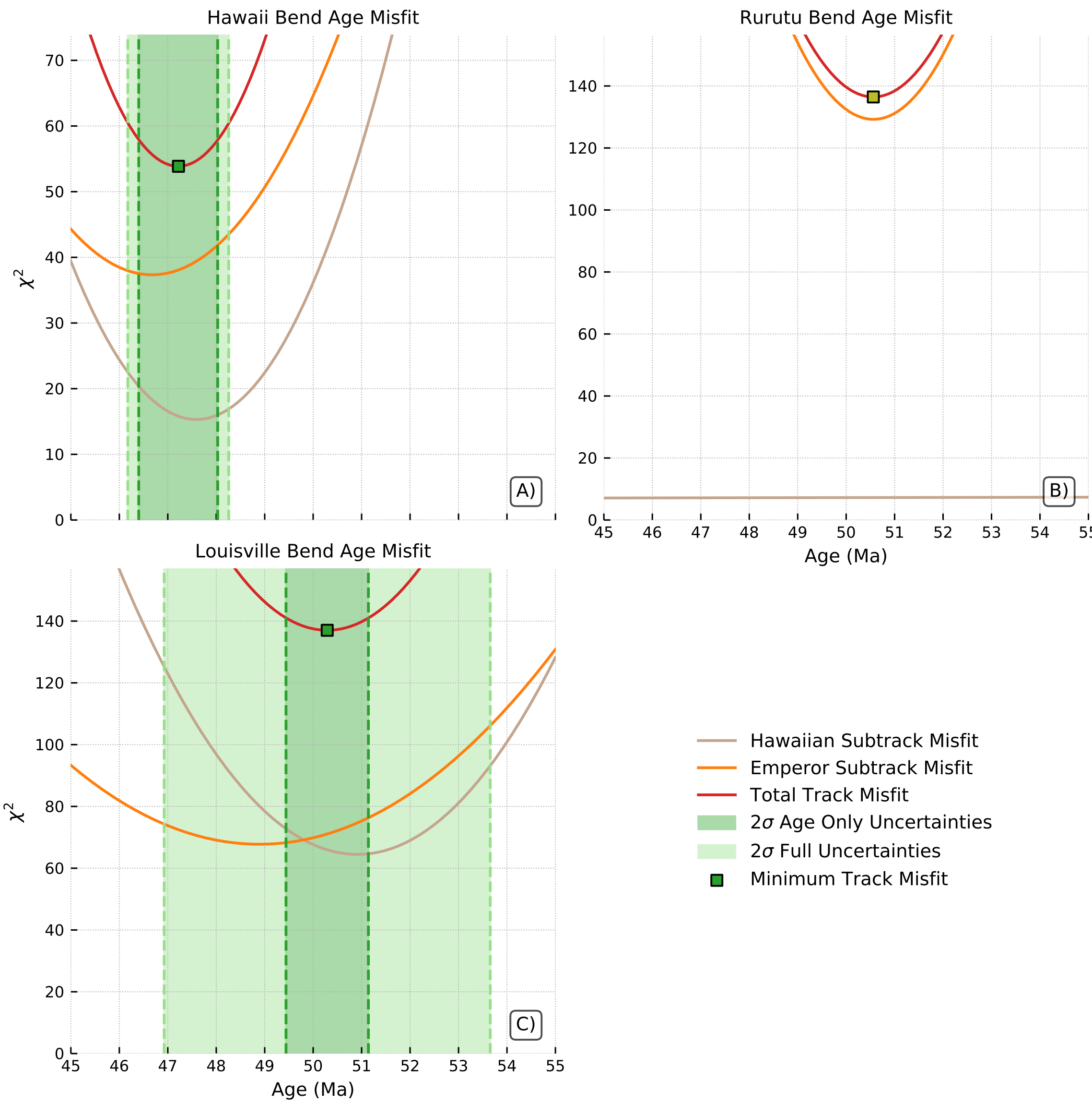

Figure S4. Sum-squared normalized misfit (SSNM) versus bend age for each Pacific hotspot chain. Tan and orange curves respectively are the contribution of the Hawaiian age and Emperor age subtracks to the SSNM for each chain. Rurutu is excluded from the combined estimate because its bend cannot be geographically determined independently of other hotspot tracks.

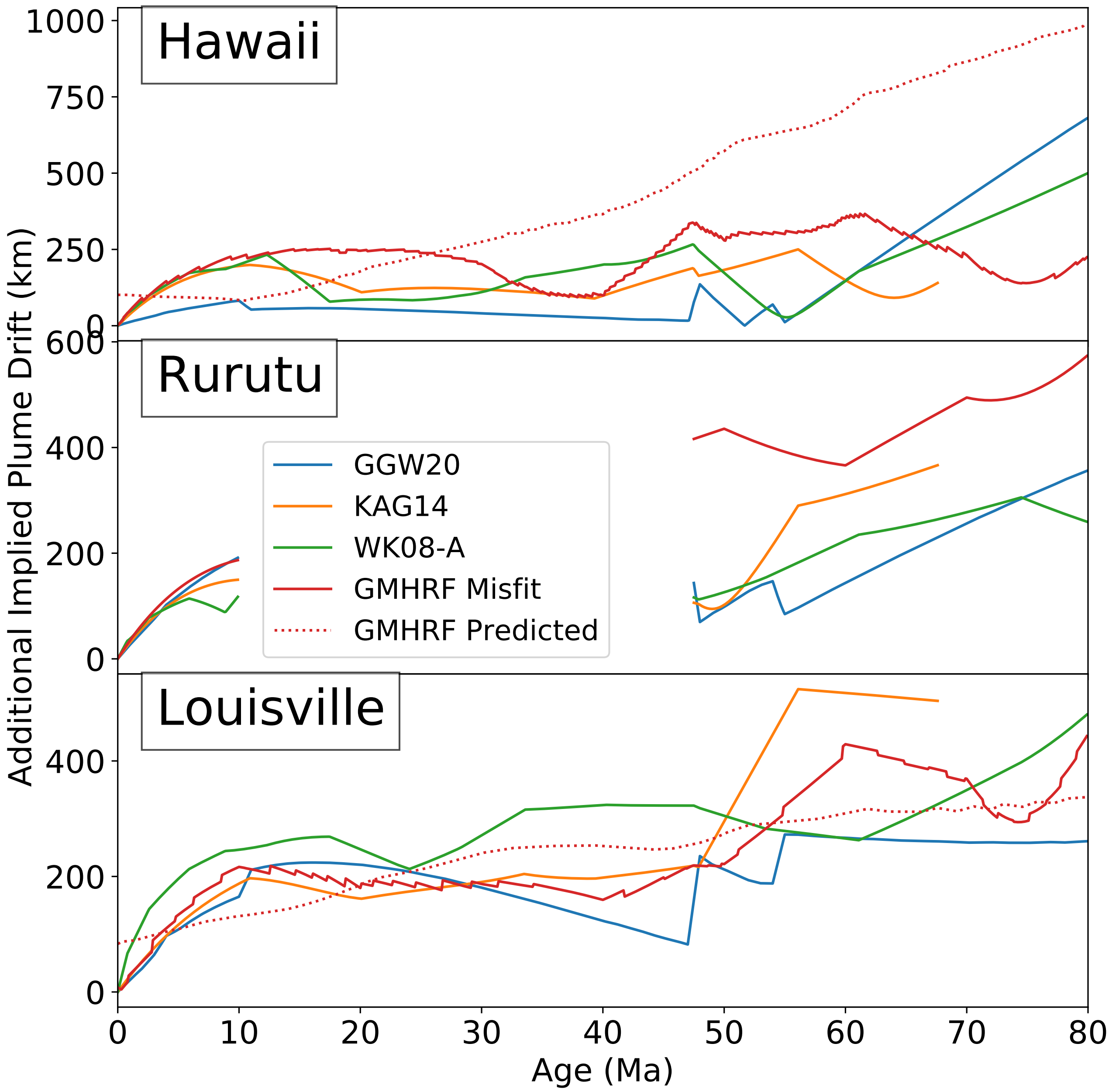
Hawaii
Rurutu
Louisville
GGW20
KAG14
WK08-A
GMHRF Misfit
GMHRF Predicted
Additional Implied Plume Drift (km)
Age (Ma)
1000
750
500
250
0
600
400
200
0
400
200
0
0
10
20
30
40
50
60
70
80

Figure S5. Distance misfit to hotspot models. For Pacific plate rotations relative to assumed-fixed hotspots (GGW20 (this study), KAG14 (Koivisto et al., 2014), and WK08-A (Wessel & Kroenke, 2008)), this is the misfit of our preferred age models to the fixed hotspot approximation (blue, green, and orange curves). For the "Global Moving Hotspot Reference Frame" (GMHRF) (Doubrovine et al., 2012), this is the misfit of our preferred age models to the motion they predict for Hawaii and Louisville; for Rurutu (which they do not model), we show the misfit as if Rurutu were fixed in the GMHRF (solid red curves). Dotted red curve shows the magnitude of motion predicted for Hawaii and Louisville by Doubrovine et al. (2012).

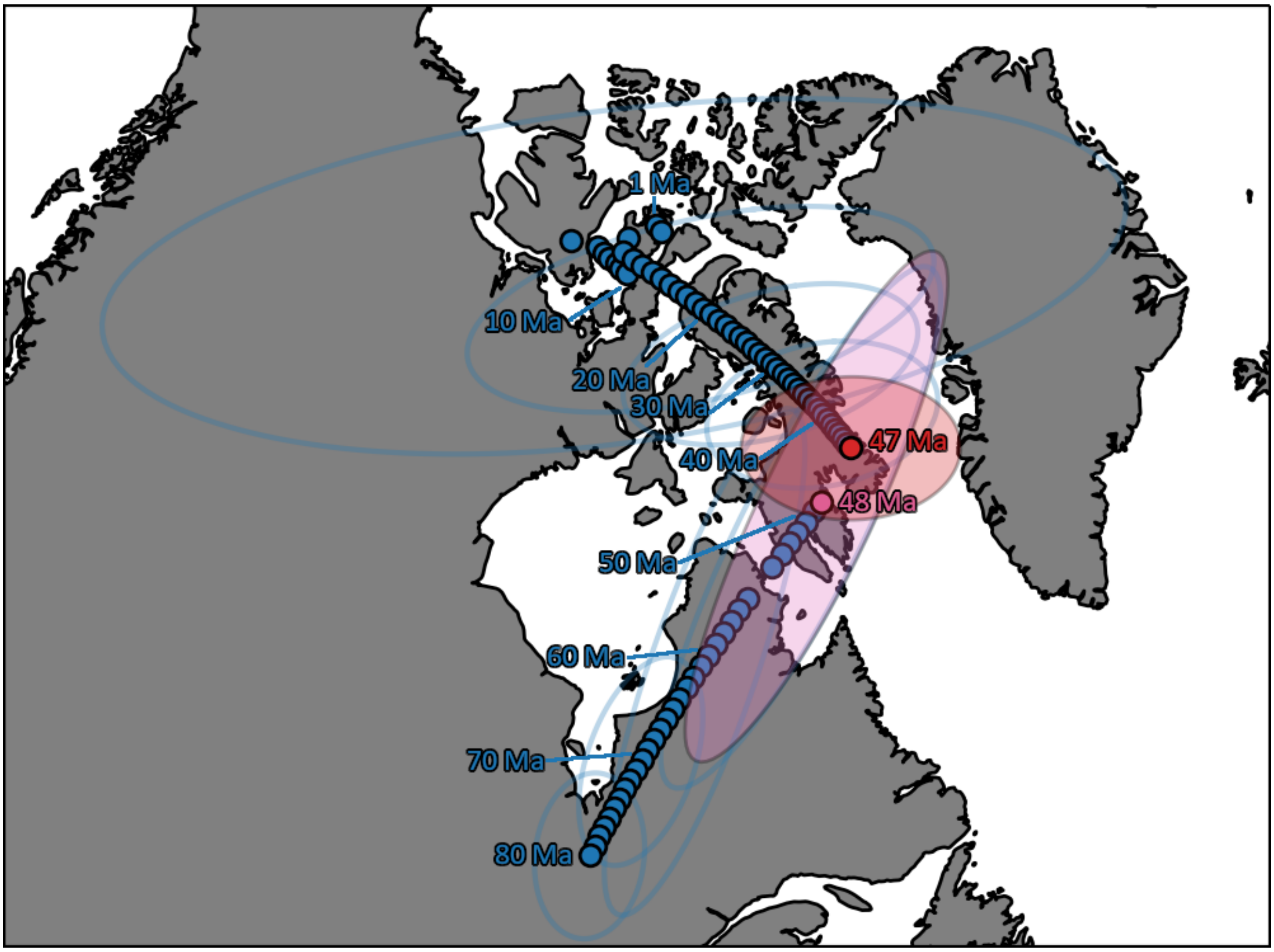

Figure S6. Poles of finite rotation and uncertainties from applying the N-hotspot method (Andrews et al., 2006) to our age models for the Hawaiian-Emperor, Louisville, and Rurutu hotspots. The red pole is the oldest Hawaiian subtrack finite rotation pole (47 Ma) and the pink pole is the youngest Emperor subtrack finite rotation pole (48 Ma). The blue reconstruction poles on either side are spaced in 1 Ma intervals with the youngest being for 40 Ma and the oldest being for 55 Ma.

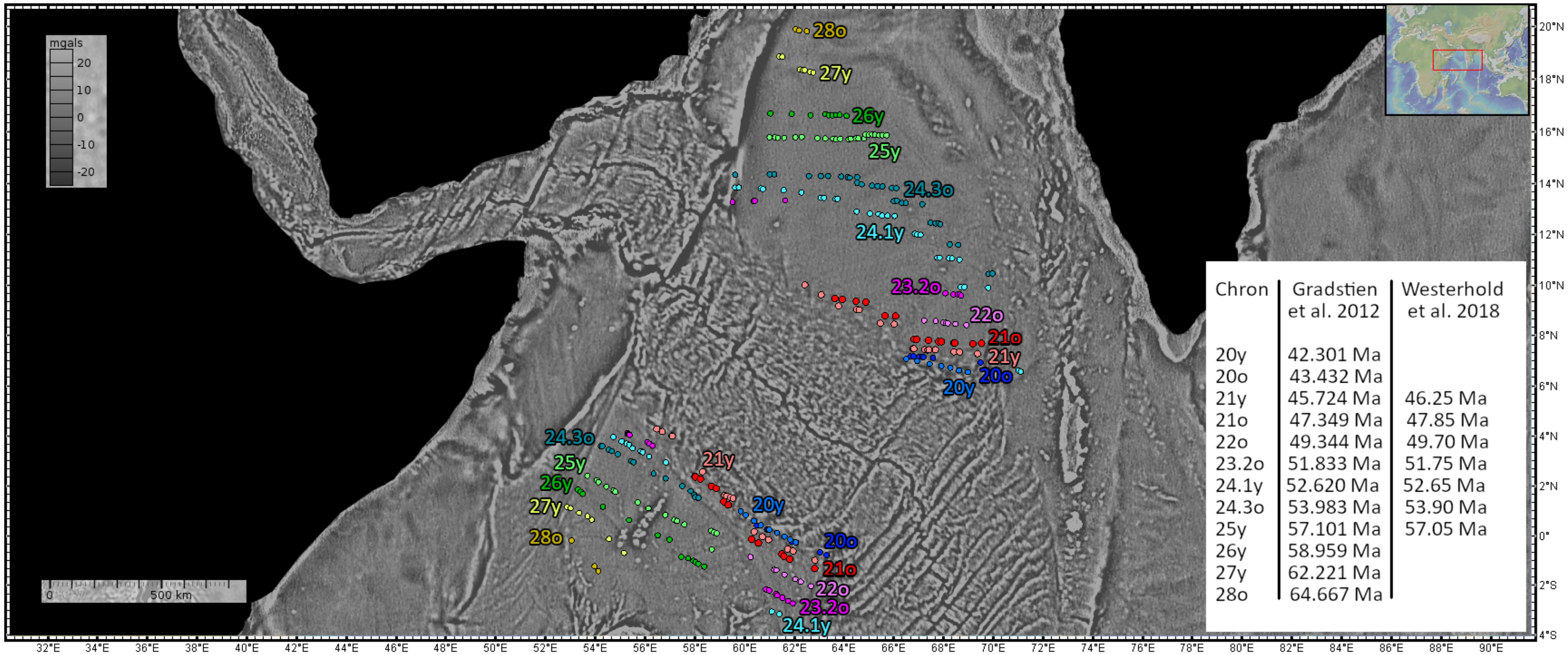

Figure S7. Transition from smooth to rough seafloor, representing a sudden and substantial decrease in spreading rates, flanking the Carlsberg Ridge. Isochrons from Cande et al. (2010) for 20y to 23.2o and Eagles and Hoang (2014) for 24.3o to 28o are plotted atop the vertical gravity gradient of Sandwell et al. (2014) and show that the smooth to rough transition occurred near 21o–21y.

	Hawaiian-Emperor				Rurutu				Louisville			
Bend Location	ML Lat.	ML Lon.	σ_{geo}	ν	ML Lat.	ML Lon.	σ_{geo}	ν	ML Lat.	ML Lon.	σ_{geo}	ν
	32.7°N	171.7°E	35 km	57	6.4°S	177.4°E	72 km	17	37.1°S	169.5°W	21 km	71
					Fin Lat.	Fin Lon.			C Lat.	C Lon.		
					8.6°S	178.5°E			38.0°S	168.5°W		
Hawaiian-Age												
Subtrack	ML Lat.	ML Lon.	ML Radius		ML Lat.	ML Lon.	ML Radius		ML Lat.	ML Lon.	ML Radius	
	68.1°N	112.9°W	54.5°		59.2°N	96.0°W	93.7°		2.0°N	131.3°W	52.8°	
					Fin Lat.	Fin Lon.	Fin Radius		C Lat.	C Lon.	C Radius	
					64.0°N	77.7°W	103.6°		1.1°N	131.7°W	51.7°	
Emperor-Age												
Subtrack	Lat.	Lon.	Radius		ML Lat.	ML Lon.	ML Radius		ML Lat.	ML Lon.	ML Radius	
	12.5°N	107.6°E	61.5°		21.2°N	125.7°W	62.2°		25.7°N	82.7°W	102.8°	
					Fin Lat.	Fin Lon.	Fin Radius		C Lat.	C Lon.	C Radius	
					23.7°N	112.7°W	74.5°		4.9°N	115.5°W	65.2°	

Table S1. Abbreviations: ML Lat., maximum likelihood latitude of bend or small circle pole fit to ML bend; Lon., maximum likelihood longitude of bend or small circle pole fit to ML bend; Fin Lat., latitude of Rurutu bend from Finlayson et al. (2018) or latitude of small circle pole fit to that bend; Fin Lon., longitude of Rurutu bend from Finlayson et al. (2018) or longitude of small circle pole fit to that bend; C Lat., coeval Louisville bend latitude or latitude of small circle pole fit to that bend; C Lon., coeval Louisville bend longitude or longitude of small circle pole fit to that bend; σ_{geo}, standard deviation of volcano locations about best-fitting small circles; ν, degrees of freedom (the number of volcanoes used minus the number of adjustable parameters); An F-ratio test shows that σ_{geo} differs significantly between hotspot tracks: $p = 2 \times 10^{-5}$ for Hawaii compared with Rurutu, $p = 3 \times 10^{-5}$ for Louisville compared with Hawaii, and $p = 2 \times 10^{-14}$ for Louisville compared with Rurutu.

	Degree	Hawaii				Rurutu				Louisville			
		χ^2	DOF	F-Value	P-Value	χ^2	DOF	F-Value	P-Value	χ^2	DOF	F-Value	P-Value
Hawaiian Subtrack	1	67.07	19	N/A	N/A	6.92	3	N/A	N/A	93.92	18	N/A	N/A
	2	15.30	18	60.88	3.49E-07	6.82	2	0.03	0.88	64.47	17	7.76	0.01
	3	13.02	17	2.98	0.10	6.38	1	0.07	0.84	58.94	16	1.50	0.24
Emperor Subtrack	1	37.34	5	N/A	N/A	129.23	16	N/A	N/A	67.75	6	N/A	N/A
	2	16.44	4	5.09	0.09	97.64	15	4.85	0.04	67.75	5	0.00	0.99

Table S2. F-tests for the addition of another parameter done on polynomial age models. Degree indicates the degree of the polynomial fit to the indicated subtrack and chain. χ^2 is the SSM for the least squares polynomial fit. DOF is the degrees of freedom of the model. F-value is the F-statistic used in this test and corresponds to $\frac{\chi^2(m)-\chi^2(m+1)}{\chi^2_\nu(m+1)}$ where $\chi^2(m)$ is the SSM of the original model with m parameters, $\chi^2(m+1)$ is the SSM of the model with an additional parameter, and $\chi^2_\nu(m+1)$ is the SSNM of the model with an additional parameter. P-Value is the corresponding P-Value of the test statistic shown in the F-Value column for an F-distribution with 1 by m+1 degrees of freedom.

Hotspot Track	Subtrack	Quadratic	Linear	Constant	a	b	c	d	e	f
Hawaiian-Emperor	Hawaii	0.018	0.89	0.49	5.3E-06	-1.6E-04	-1.6E-04	5.4E-03	-2.1E-02	1.6E-01
	Emperor		1.43	1.54				2.3E-02	-8.9E-01	3.5E+01
Rurutu	Hawaii	0.016	0.90	0.30	9.3E-03	-8.4E-02	5.0E-02	7.9E-01	-6.1E-01	1.6E+00
	Emperor		1.98	-17.87				2.7E-02	-1.0E+00	3.9E+01
Louisville	Hawaii	0.022	1.35	1.78	7.8E-05	-2.2E-03	1.1E-02	6.5E-02	-3.8E-01	3.1E+00
	Emperor		2.16	-4.91				8.3E-02	-2.7E+00	9.2E+01

Table S3. Age model parameters inverted for in coeval bend age model shown in Figure 2 for all three hotspot tracks included in this study. The full 3D covariance matrix for the quadratic case is shown in equation 1 below and the 2D covariance matrix determined for the linear models is given by the lower right 2x2 submatrix. The covariance matrix is ordered so **a** represents the quadratic variance and the trace descends in order.

$$CovarianceMatrix = \begin{pmatrix} a & b & c \\ b & d & e \\ c & e & f \end{pmatrix} \tag{1}$$

Hotspot Track	Subtrack	Quadratic	Linear	Constant	a	b	c	d	e	f
Hawaiian-Emperor	Hawaii	0.017	0.90	0.45	5.5E-06	-1.7E-04	5.7E-04	5.6E-03	-2.2E-02	1.7E-01
	Emperor		1.45	0.58				2.2E-02	-8.5E-01	3.4E+01
Rurutu	Hawaii	0.020	0.86	0.32	9.4E-03	-8.5E-02	5.0E-02	8.0E-01	-6.2E-01	1.6E+00
	Emperor		1.68	-4.87				1.5E-02	-5.7E-01	2.2E+01
Louisville	Hawaii	0.021	1.37	1.67	7.9E-05	-2.2E-03	1.1E-02	6.5E-02	-3.8E-01	3.2E+00
	Emperor		2.12	-3.82				8.4E-02	-2.8E+00	9.3E+01

Table S4. Age model parameters inverted for in independent bend age model shown in Figure S1 for all three hotspot tracks included in this study. The full 3D covariance matrix for the quadratic case is shown in equation 2 below and the 2D covariance matrix determined for the linear models is given by the lower right 2x2 submatrix. The covariance matrix is ordered so **a** represents the quadratic variance and the trace descends in order.

$$CovarianceMatrix = \begin{pmatrix} a & b & c \\ b & d & e \\ c & e & f \end{pmatrix} \tag{2}$$

Table S5. Locations, ages, and meta data of seamounts used in this study to define the geographic and age progressions of the Hawaiian, Rurutu, and Louisville hotspots. Latitude and Longitude columns define the geographic position of the seamount high. The age is given in Ma and the 2-sigma column represents the uncertainty on that age in Ma^2. The Seamount column gives the name of the seamount and citations for the seamount information are given under the source column. The method and sampling columns describe the dating method and sampling techniques used to obtain the age information. The "Include" column is labeled y for "yes" when data which was incorporated in the study and n for "no" when data was excluded. The "Age Span" column which exists for the Louisville sheet only describes if the age 2-sigma uncertainty represents an age span as reported in Heaton and Koppers (2019) or whether an analytic uncertainty on the date reported.

Table S6.

[a] Reconstructions of the Pacific plate relative to Pacific hotspots every 1 Ma between 80 Ma and the present. Dividing by $\hat{\kappa}$, as shown in note b, makes χ^2_ν=1 which corrects for the over-dispersion of the problem but is not required if a more conservative estimate of uncertainty is desired.

[b]

$$CovarianceMatrix = \frac{1}{\hat{\kappa}} \begin{pmatrix} a & b & c \\ b & d & e \\ c & e & f \end{pmatrix} \times 10^{-5} radians^2 Ma^{-2} \tag{4}$$

Table S7. Table of the ages of Eocene tectonic events mostly in the Pacific and Indian Ocean Basins. The region column breaks down the event broadly by region in the world or global depending on location of occurrence. The event column gives a brief 1 sentence description of the event in question. Start age and stop age are given in units of millions of years and list either the age range of the event in question or $\pm 2\sigma$ of its mean age. The constraint type column gives a bit more detail on how the age of the event is constrained. The citation column lists the citations used to come up with the age range and event listed.